Department of Physics and Astronomy
University of Heidelberg

Master Thesis in Physics
submitted by

Charlotte Maria König

born in Port Huron (USA)

2019

In-trap Laser Desorption in an EBIT for the Production of Highly Charged Ions of Rare Isotopes at Pentatrap

This Master Thesis has been carried out by Charlotte Maria König at the
Max-Planck-Institute for Nuclear Physics in Heidelberg
under the supervision of
Prof. Dr. Klaus Blaum

Abstract

Highly charged ions (HCI) are important for precision measurements in fundamental physics, for example, they increase the precision of Penning-trap mass spectrometry (PTMS) since the relative uncertainty scales with the charge of the ion. The production of HCI without the need of large scale facilities is realized by electron beam ion traps (EBITs) [1]. This thesis reports on the optimization of a novel, highly-efficient loading scheme for rare isotopes in EBITs, namely in-trap laser desorption in a Heidelberg compact EBIT (HC-EBIT) [2], the Tip-EBIT. The production and subsequent extraction of HCI of ^{165}Ho, using sample sizes as small as 10^{12} atoms (about 270 pg), is demonstrated for charge states up to 47+. The target could be used for several ten thousand laser shots with an overall production of more than 10^7 ions of a single charge state. Additionally, hydrogen-like calcium ($^{40}Ca^{19+}$) has been produced and extracted, demonstrating the applicability of the loading technique for lighter elements. In the course of this thesis, the Tip-EBIT was attached to the PENTATRAP PTMS experiment, as a source for HCI of rare isotopes. The first measurement will be the mass-ratio determination of ^{163}Ho and ^{163}Dy, for which FAC calculations were carried out within this thesis to avoid charge states with low-lying metastable atomic states. This will contribute an independent value of the energy available for the electron capture decay (Q_{EC}-value) of this rare holmium isotope to the ECHo collaboration. The aim of the collaboration is the determination of the electron neutrino mass on the sub-eV level [3].

Zusammenfassung

Hochgeladene Ionen (HCI) sind wichtig für Präzisionsmessungen in der Grundlagenforschung der Physik, z. B. verbessern sie die Präzision von Penning-Fallen Massenspektrometrie (PTMS), da die relative Genauigkeit der Messung mit dem Ladungszustand des Ions skaliert. HCI können in Elektronenstrahl-Ionen Fallen (EBITs) [1] erzeugt werden, ohne dass experimentelle Großanlagen nötig sind. Diese Masterarbeit berichtet von der Optimierung einer neuen hocheffizienten Technik zum Laden einer EBIT mit seltenen Isotopen, der Technik der Laserdesorption in der Falle (engl. 'in-trap laser desorption') in einer 'Heidelberg compact' EBIT (HC-EBIT) [2], der Tip-EBIT. Die Erzeugung und die darauf folgende Extraktion von HCI des Elements ^{165}Ho unter Verwendung von Proben mit nur 10^{12} Atomen (etwa 270 pg) ist hier gezeigt für Ladungszustände bis 47+. Diese Probe konnte für mehrere zehntausend Laserpulse benutzt werden, wobei insgesamt über 10^7 Ionen für einen Ladungszustand erzeugt wurden. Zusätzlich wurde noch wasserstoffartiges Calcium ($^{40}Ca^{19+}$) produziert und extrahiert, wodurch die Anwendung der Ladungstechnik für leichtere Elemente demonstriert wurde. Im Verlauf dieser Arbeit wurde die Tip-EBIT an das PENTATRAP PTMS Experiment als Quelle für HCI seltener Isotope angeschlossen. Die erste Messung mit der neuen Quelle wird die Bestimmung des Massenverhältnisses von ^{163}Ho und ^{163}Dy sein, wofür in dieser Arbeit FAC Berechnungen durchgeführt wurden um Ladungszustände mit niederenergetischen metastabilen Zuständen zu vermeiden. Hiermit wird ein unabhängiger Wert der freiwerdenden Energie des Zerfalls durch Elektroneneinfang (Q_{EC}-Wert) dieses seltenen Holmium-Isotops der ECHo-Kollaboration zur Verfügung gestellt werden. Diese Kollaboration hat sich zum Ziel gesetzt, die Elektron-neutrino Masse im sub-eV Bereich zu bestimmen [3].

Contents

Chapter 1

Introduction

Most of the matter of the universe is made up of highly charged ions (HCI) [4], which is why the scientific study of HCI is important for a wide field of physics. This ranges from applications in astrophysics [5] and plasma physics [6] to tests of QED [7, 8] and other fundamental physics, such as the variation of fundamental constants [9]. For example, the interest of high-precision spectroscopy and novel optical clocks using HCI has strongly increased, due to their high sensitivity to a potential time-dependence of the fine-structure constant α [10] and effects of dark matter candidates [11]. Additionally, HCI are less sensitive to external perturbations because of their compact size, compared to neutral atoms or singly charged ions [9].

Another application of HCI in fundamental physics are Penning-trap experiments, in which the ion's frequencies in the superimposed electric and magnetic fields can be determined with a very high precision. Such experiments include the g-factor measurements at ALPHATRAP for testing QED [7] and high-precision mass spectrometry e.g. at SMILETRAP [12], TITAN [13], and PENTATRAP [14]. High-precision Penning-trap mass spectrometers employ HCI to increase the relative precision with which the free-space cyclotron frequency can be determined, as it scales linearly with the ion's charge.

Currently, the first measurement results of the high-precision Penning-trap mass-spectrometer PENTATRAP are being published. Mass ratios of several xenon isotopes demonstrate a precision of close to 10^{-11} and an eV/c^2 accuracy, novel for ions with $Z > 50$ [15]. The mass-ratio measurement of ^{187}Re and ^{187}Os is of interest for neutrino physics due to the β-decay of rhenium to osmium in which an electron anti-neutrino is emitted. A combination of a calorimetric measurement of the decay spectrum and a measurement of the energy difference of the ground states of the mother and daughter nuclei (Q-value) by high-precision Penning-trap mass spectrometry will lead to an upper limit of the mass of the electron anti-neutrino [16]. At PENTATRAP this measurement led to the detection of atomic metastable excited states in HCI [17]. On the one hand, this opens up the possibility to detect such states in Penning traps e.g. for high-precision clocks using HCI, but on the other hand, the metastable states can negatively influence the accuracy of mass-ratio measurements [16]. Based on this discovery, calculations using Flexible Atomic Code (FAC) were carried out for holmium and dysprosium in the work of this thesis. The calculations yield low-lying metastable states for some charge states at excitation energies as low as 4 eV. For a precise mass-ratio determination it is important to avoid the charge states featuring these low-lying states,

however, they can also be used to demonstrate the high precision of PENTATRAP by resolving the energy difference of the ground state and such an excited one.

For the xenon, rhenium, and osmium measurements naturally abundant isotopes were used, for which the production efficiency of a commercial DreEBIT [18] with the injection of gas or volatile compounds via the MIVOC technique [19] was sufficient.

The next measurement campaign planned at PENTATRAP is the mass-ratio determination of ^{163}Ho and ^{163}Dy, as part of the electron capture in holmium (ECHo) collaboration [3]. The ECHo collaboration aims at the determination of the electron neutrino mass in the sub-eV range. The current upper limit for the electron neutrino mass is $m_{\nu_e} < 150\,\mathrm{eV/c^2}$ (95 % C.L.) [20], while the upper limit of the mass of the electron anti-neutrino has recently been determined more precisely by the KATRIN experiment to a value of $m_{\bar{\nu}_e} < 1.1\,\mathrm{eV/c^2}$ (90 % C.L.) [21].

To achieve such a low upper limit of the electron neutrino mass, the ECHo experiment exploits the electron capture (EC) decay of ^{163}Ho to ^{163}Dy:

$$^{163}\mathrm{Ho} \rightarrow\ ^{163}\mathrm{Dy}^{*} + \nu_e \rightarrow\ ^{163}\mathrm{Dy} + \nu_e + Q_{\mathrm{EC}}\ , \tag{1.1}$$

where Q_{EC} is the total energy available for the decay. For the experiment, ^{163}Ho is implanted in the absorber material of a metallic, magnetic calorimeter. As it decays the de-excitation spectrum of ^{163}Dy* is measured via the emitted x-rays and Auger electrons. The region of the spectrum most sensitive to the neutrino mass is the endpoint region in which the x-rays and Auger electrons carry most of the energy and the neutrino only its rest mass and no kinetic energy. The decay spectrum is fitted with a theoretical model yielding Q_{EC} and m_{ν_e}. Precise knowledge of the Q_{EC}-value is essential to account for systematics, which is why PENTATRAP will contribute an independent Q_{EC}-value with a high-precision measurement of the mass difference of ^{163}Ho and ^{163}Dy. To achieve the goal of the electron neutrino mass on the sub-eV level, the Q_{EC}-value must be determined with a precision of better than 1 eV which corresponds to a relative mass-ratio uncertainty of less than $6 \cdot 10^{-12}$. This precision is only feasible with mass spectrometry of HCI in the Penning-trap setup at PENTATRAP.

To make this measurement possible, HCI of the radioactive isotope ^{163}Ho have to be produced, transported to, and loaded into the Penning traps. Due to the synthetic nature of this isotope, only a limited amount of 10^{14} atoms (about 27 ng) is available for the measurement at PENTATRAP, requiring a very efficient production of HCI.

Before 1988, HCI could be produced only at large research facilities such as particle accelerators (e.g. at the ESR facility at GSI [22]), with the use of multi-joule terawatt lasers [23] or employing techniques such as the sliding spark method [24] which are however of limited ability [23]. Electron-cyclotron resonance ion sources (ECRIS) [25], electron-beam ion sources (EBIS) [26], and electron-beam ion traps (EBIT) [1] present the next generation of sources for HCI, producing high charge states without the need of large scale facilities.

There are several options for loading atoms into an EBIT for the production of HCI of a certain element. These include the injection of a gas or a volatile compound whenever available and external laser ablation sources with additional transport to the EBIT. Both techniques require a large quantity of sample material ($> 0.1\,g$) for the production of HCI, which can be problematic for certain isotopes that are rare, expensive or hazardous. A loading technique has been developed for these rare isotopes,

namely the wire probe injection, with which HCI of uranium were produced using a sample of 100 ng of ^{233}U [27]. The focus of this experiment was on the production of HCI and not on the subsequent extraction which was therefore not demonstrated. A Heidelberg compact EBIT (HC-EBIT) [2] employing the wire probe technique was tested at PENTATRAP as a possible source for HCI of rare species. However, in this case, the technique could not produce HCI in the EBIT [28]. To provide a more efficient loading scheme allowing subsequent extraction of the HCI, the in-trap laser desorption technique was developed in the same HC-EBIT, the Tip-EBIT, to which this thesis is dedicated. With this loading scheme in the Tip-EBIT, HCI of ^{165}Ho have been produced and ejected, using samples containing only 10^{12} holmium atoms, which corresponds to about 270 pg. Among others, these measurements will be presented in this thesis.

The determination of the Q_{EC}-value of the decay of ^{163}Ho is not the only measurement planned at PENTATRAP for which HCI of rare isotopes are required. For example, high-precision Penning-trap mass spectrometry of chlorine isotopes, where one isotope (^{36}Cl) is only available in minute quantities, can be used to test special relativity by comparing the mass difference of two isotopes to the energy emitted in neutron capture of the lighter one [29, 30]. Additionally, mass measurements of calcium isotopes will contribute to precision isotope shift spectroscopy for a King plot analysis. Without new physics the shift of the transition frequencies of the isotopes is linear, therefore detection of a non-linearity can set limits on or even lead to evidence of dark matter [31]. For this purpose, loading of a natural calcium composition using in-trap laser desorption in the Tip-EBIT has been successfully tested, demonstrating the application of this technique also for elements considerably lighter than holmium and dysprosium.

Structure of this thesis

In this thesis, chapter 2 describes the working principle of EBITs in general. Then, chapter 3 presents the results of an FAC calculation determining atomic metastable states of holmium and dysprosium for several charge states, which can be used for the selection of suitable charge states for the mass-ratio measurements of these two elements. In the following, chapter 4 describes the experimental setup used for optimization of the in-trap laser desorption in the Tip-EBIT (test setup) and gives a brief introduction to the PENTATRAP experiment to which the Tip-EBIT is now attached. Finally, chapter 5 presents the results obtained with the test setup and the successful attachment of the Tip-EBIT to the PENTATRAP beamline, where it will soon be used as the source for HCI of ^{163}Ho and ^{163}Dy.

Chapter 2

Working principle of electron beam ion traps

The electron beam ion trap (EBIT) was developed in 1988 by Levine [1, 32] at the Lawrence Livermore National Laboratory and has since evolved to an irreplaceable device for the production and study of highly charged ions (HCI). EBITs can produce and trap HCI of elements in a wide mass range while the charge state distribution is controllable. There is a large variety of EBITs depending on which species and charge state range is required. It spans from small room temperature devices to large liquid helium-cooled EBITs that can produce bare uranium ions (U^{92+}) using an electron beam energy of 200 keV [33]. EBITs can be used as a source of HCI for other experiments without the need for large facility setups such as high-energy accelerators or storage rings. This leads to a vast field of applications wherever HCI are needed as in our case mass measurements at PENTATRAP.

First, I will give an overview of the main components and their purpose (section 2.1). section 2.2 is dedicated to the physical processes occurring in an EBIT that alter the charge state of the ions and in the end, in section 2.3 a short description of evaporative cooling is given.

2.1 General principles

The main process leading to the production of HCI in EBITs is electron impact ionization. This requires a highly energetic and dense electron beam to efficiently remove electrons bound in atoms. The basic components necessary to produce such an electron beam are the electron gun, the trap electrodes, and the electron collector whereby the trap electrodes are situated in a strong, inhomogeneous magnetic field. They are shown schematically in Figure 2.1.

The electron gun contains a heated cathode, which emits electrons that are then accelerated towards the trap electrodes by applying a negative voltage to the cathode and a positive one to the anode creating a beam of electrons. The beam is then further accelerated by an even higher positive voltage applied to the electrodes. The magnetic field is strongest in the center at the trap electrodes and decreases towards the electron gun as well as the collector, with both ideally lying in a field-free region. The magnetic field lines are sketched in Figure 2.1.

The electrons are subject to the Lorentz force of the magnetic field causing them to follow a circular orbit transverse to the magnetic field with radius r_e. Due to the conservation of the magnetic flux, r_e decreases as the magnetic field increases [34]. This leads to a strong radial compression of the electron beam in the center of the trapping region, increasing the electron beam density. Following the magnetic field lines, the electron beam radius increases again when exiting the trap region towards the collector. In addition, a negative voltage is applied to an electrode following the collector, prohibiting any electrons from leaving the EBIT.

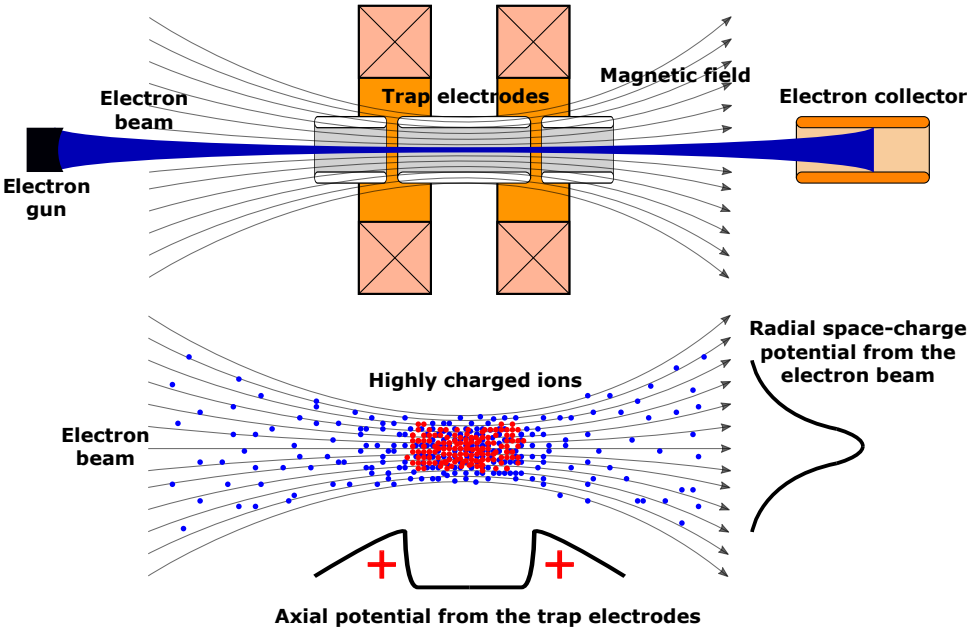

Figure 2.1: The upper schematic shows the main parts of an EBIT: the electron gun, the three trap electrodes, and the electron collector. In addition, the electron beam (blue) and its compression due to the magnetic field are shown. The bottom part illustrates the confining potentials: the voltages applied to the trap electrodes (axial) and the space charge potential of the electron beam (radial). The ions in the trapping region are indicated as red dots. Taken from [28].

The energy of the electrons is roughly defined by the potential difference of the cathode and the central trap electrode:

$$E_\mathrm{e} \approx e(U_\mathrm{center} + |U_\mathrm{cathode}|) \; . \tag{2.1}$$

The energy of the electron beam is increased by the potential of the trapped positive ions (Φ_ions) and decreased by the work function of the cathode material (Φ_w) and the space charge potential of the electron beam itself (Φ_e). In total the electron beam energy can be given by [34]:

$$E_\mathrm{e} = e(U_\mathrm{center} + |U_\mathrm{cathode}| + \Phi_\mathrm{ions} + \Phi_\mathrm{w} + \Phi_\mathrm{e}) \; , \tag{2.2}$$

where Φ_w and Φ_e are defined negatively.

Flexibility in the energy of the electron beam is essential since the electron binding energy varies strongly depending on the charge state of the ion. Meaning that the electron beam energy is one of the parameters determining the charge states of the ions. When the electron beam energy is lower than the energy required to remove the next electron, the higher charge state will not be reached. Figure 2.2 shows the ionization energies for a selection of elements as a function of the charge state, showing the wide range of electron beam energies needed depending on the element and charge state of interest. Not only does the energy necessary to further ionize increase, but the ionization cross section also decreases as the charge state increases, empirically described by the Lotz cross section [35]. This implies that also a stronger magnetic compression of the beam is necessary as this increases the electron beam density.

The compression of the electron beam can be described by the optical theory of Herrmann [36]. By definition, the Herrmann radius r_h^e is the radius through which 80 % of the beam passes. It is given by [37]:

$$r_h^e = r_b^e \sqrt{\frac{1}{2} + \frac{1}{2}\sqrt{1 + 4\left(\frac{8 m_e k_b T_c r_c^2}{e^2 r_b^4 B^2} + \frac{B_c^2 r_c^4}{B^2 r_b^4}\right)}} \,, \tag{2.3}$$

where r_b is the Brillouin radius [38], given by [37]:

$$r_b^e = \sqrt{\frac{2 m_e I_e}{\pi \epsilon_0 v_e e B^2}} \,, \tag{2.4}$$

m_e the mass and e the charge of the electron, k_b the Boltzmann constant, T_c the temperature and r_c the radius of the cathode, B_c the strength of the magnetic field at the cathode and B at the position of interest, I_e the electron beam current, and $v_e = \sqrt{\frac{2eU}{m_e}}$ the velocity of the electrons with the acceleration voltage U and ϵ_0 the vacuum permittivity.

The electrostatic potential confining the ions in the axial direction is realized by applying a lower positive voltage to the central trap electrode compared to the outer two electrodes (V_{trap}), resulting in a potential well as indicated in Figure 2.1. In addition, the space charge of the electron beam creates a confinement in radial direction (V_{sc}), resulting in a potential which confines the ions in all three spatial directions. The space charge of the positive ions ($\sum_i V_i$) in charge states i, as well as the image charge of the electron beam on the trap electrodes (V_{ic}) additionally affect the trapping potential [40]:

$$V(\rho, z) = V_{\mathrm{trap}}(\rho, z) + V_{\mathrm{sc}}(\rho) + V_{\mathrm{ic}}(\rho, z) + \sum_i V_i(\rho, z) \,, \tag{2.5}$$

with ρ being the radial and z the axial coordinates.

2.2 Interaction processes of the electron beam and the ions

Several processes occurring in an EBIT can alter the charge state of the trapped ions. They can be divided into two categories: interaction of the atoms and ions with the

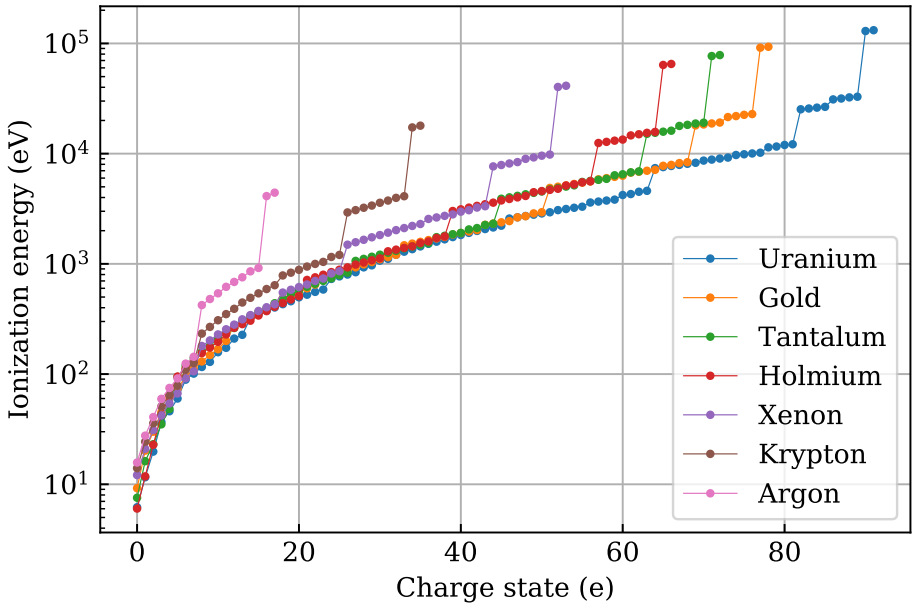

Figure 2.2: Ionization energy as a function of the charge state for a selection of seven elements. The elements were chosen to cover a broad mass range thus depicting the wide range of ionization energies arising for different atomic numbers. The figure is adapted from [28, 39].

electron beam and interaction of the ions with each other. Figure 2.3 illustrates the four interaction processes of the ions with the electron beam. The most fundamental process for EBITs is electron impact ionization (EI). As Figure 2.3a shows an electron formerly bound is removed from either an atom or an ion:

$$A^{i+} + e^- \longrightarrow A^{(i+1)+} + 2e^- \ . \tag{2.6}$$

This can only occur if the energy of the electron beam is at least as large as the ionization potential which has to be overcome to remove the electron, limiting the charge state that can be reached. The process is most efficient when the energy of the electron beam is about three times the value of the ionization potential [35].

On the other hand an electron from the beam can also be captured back into an empty shell of an ion under the emission of a photon, which is then the process of radiative recombination (RR) (Figure 2.3b):

$$A^{i+} + e^- \longrightarrow A^{(i-1)+} + \hbar\omega \ . \tag{2.7}$$

The emitted photon carries the kinetic energy of the electron and the energy gained by the recombination, the ionization potential Φ_{ip} : $\hbar\omega = E_{\mathrm{e}} + e\Phi_{\mathrm{ip}}$.

The other two processes depicted in Figure 2.3 produce photons at energies characteristic to the species ionized in the EBIT. As indicated, the photon energies correspond to the energy differences of electron shells. These x-ray photons can then be detected giving a non-destructive method to analyze the species of the trapped ions. The processes are electron impact excitation (EE) and dielectronic recombination (DR). In EE energy from a beam electron is transferred to a bound one in an elastic collision but

only so much as to excite but not further ionize (Figure 2.3c). The excited ion then emits a photon and goes back to ground state:

$$A^{i+} + e^- \longrightarrow (A^{i+})^* + e^- \longrightarrow A^{i+} + \hbar\omega + e^- \ . \tag{2.8}$$

When a beam electron is captured in an empty shell of an ion the energy, instead of being released as in RR, can be converted by lifting a bound electron to a higher atomic shell. The ion is then in an excited state that decays under the emission of a photon, which is the process of DR shown in Figure 2.3d. This is a resonant process since the energy of the electron beam has to have a value corresponding to the electron shell transition: $E_\mathrm{e} + e\Phi_\mathrm{ip} = \hbar\omega$:

$$A^{i+} + e^- \longrightarrow (A^{(i-1)+})^* \longrightarrow A^{(i-1)+} + \hbar\omega \ . \tag{2.9}$$

Other than interacting with the electron beam, ions and atoms in the trapping region can also interact with each other, for example, interactions of trapped ions and rest gas atoms. When an ion and an atom or an ion of lower charge collide electrons can be transferred to the higher charged ion. This is then a charge exchange process (CE):

$$A^{i+} + B^{j+} \longrightarrow A^{(i-x)+} + B^{(j+x)+} \ , \tag{2.10}$$

where in this case A is an ion of higher charge than B ($i > j$) and x is the number of electrons transferred from B to A.

For a more thorough description of these processes including their cross sections and rates see [40]. A balance of the described processes with loading and axial and radial losses results in the population distribution of the charge states.

2.3 Evaporative cooling

In ion-ion collisions, energy is transferred from one ion to the other. Since the mean free path for ion-ion collisions in EBITs is small one can assume thermal equilibrium [1]. When taking the energy necessary for an ion of charge q to evaporate from a trap of depth V_depth into consideration [32]:

$$E_\mathrm{evap} = qV_\mathrm{depth} \ , \tag{2.11}$$

it becomes clear that low-charge ions (LCI) evaporate from the trap at lower energies than HCI. Thus in thermal equilibrium LCI may have enough energy to exit the trap while HCI do not. In this case, the LCI leave the trapping volume and thus remove energy, evaporatively cooling the HCI. It has been shown in experiments that this has a positive effect on the total number of trapped HCI and their lifetime [41]. The LCI can be injected purposely [33] or background gas can serve for the cooling effect.

Pentatrap is part of the ECHo collaboration attempting to determine an upper limit of the electron neutrino mass in the sub-eV range [3]. For this purpose, the mass ratio of ^{163}Ho and ^{163}Dy will be measured to contribute a Q-value, the energy released in the decay, for the electron capture process of holmium to dysprosium. When considering the production of HCI of these two ion species in an EBIT, it is of advantage

that they have a considerable mass and can thus achieve high charge states compared to the background gas. Due to their comparatively high charge states, they are subject to evaporative cooling by the light ions and are more easily trapped. Additionally, this has the positive effect of less background signal in the measurements because light background gas ions will have already evaporated from the trap before it is opened to release the ions of interest. The extracted ion bunch is then free of contamination concerning lighter/ less charged species.

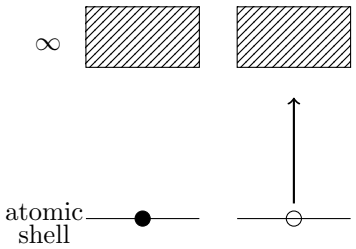

(a) Electron impact ionization (EI): an electron is removed from the atom or ion due to energy transfer from a beam electron. The charge state is increased.

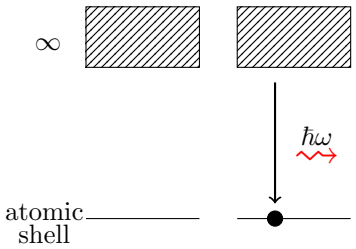

(b) Radiative recombination (RR): an electron from the electron beam is captured in an empty shell of the ion and a photon with an energy corresponding to the ionization energy of the captured electron is emitted. The charge state is decreased.

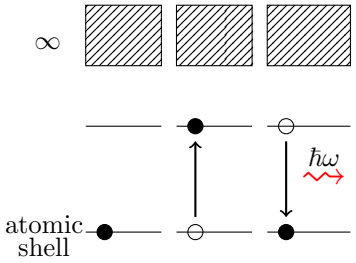

(c) Electron impact excitation (EE): energy is transferred from a beam electron to a bound one exiting it to a higher level in the ion or atom. The excited state decays via x-ray emission with the energy of the level separation.

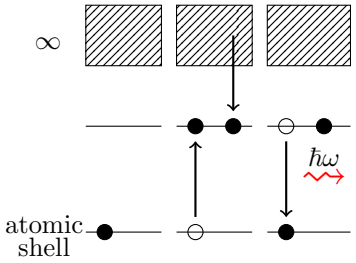

(d) Dielectronic recombination (DR): an electron is captured from the electron beam and the energy available is used to create an electronic excited state which then decays via x-ray emission. This is a resonant process as the energy of the electron beam has to equal the level transition minus the ionization energy of the captured beam electron.

Figure 2.3: Interaction processes of ions and the electron beam in an EBIT. The electrons in the beam are in the continuum depicted as dashed blocks. The filled shells of the ions that are not altered in the interaction are omitted for better clarity.

Chapter 3

Calculation of metastable states in holmium and dysprosium

An ongoing measurement campaign at PENTATRAP is the measurement of the mass ratio (R) of ^{187}Re and ^{187}Os for the determination of the Q-value of the β-decay of this rhenium isotope. While this was carried out, consistently two different values for this mass ratio were obtained [16]. For further investigation on the origin of this effect unity measurements were carried out on rhenium, where the mass ratio $^{187}\mathrm{Re}^{29+}/^{187}\mathrm{Re}^{29+}$ was determined. This also resulted in two values, the first ratio obtained was unity while the second value differed on the level of $\Delta R/R \approx 10^{-9}$. Two independent theoretical approaches and a Flexible Atomic Code (FAC) calculation reached the conclusion that some of the highly charged Re ions are produced in an excited atomic state for which the lifetime is long enough so that it is measured in the Penning traps. The lifetime of this state is predicted to be about 200 days [16], a decay has not been observed so far. Due to the long lifetime it is defined as a metastable state. From the measurement, an energy difference of 202.2(1.6) eV of the ground state of $^{187}\mathrm{Re}^{29+}$ to the metastable state could be deduced [17].

For these measurements, the DreEBIT was used as the source for the HCI of rhenium. The electronic excited states are produced in EBITs alongside the ground state due to electron impact excitation, e.g. the ion is in $[\mathrm{Kr}]4\mathrm{d}^9 4\mathrm{f}^1$ instead of the ground state $[\mathrm{Kr}]4\mathrm{d}^{10}$ in the case of the metastable state in rhenium. An explanation of the notation is given below. For an overview of the physical processes in an EBIT see section 2.2. Most of these excited states have very short lifetimes and decay along a chain of lower-lying configurations to the ground state.

In atoms and ions, the orbital angular momentum and the electron spin couple to the total angular momentum J of the system. The transition matrix defines the dependency of the transition probability on the parity and J-values of the states involved. For example, the electric dipole transition (E1) is forbidden if the transition matrix vanishes in dipole approximation. The state can then only deexcite via higher-order multipole transitions such as magnetic dipole (M1) and electric quadrupole (E2). If the transition matrix also vanishes in the next order approximation, a multipole transition of even higher order takes place (e.g. E3). This relates the difference between the J-values of the states involved (ΔJ) to a certain multipole transition. The higher the ΔJ-value is the higher the order of the lowest possible multipole for the transition

becomes. For an electric dipole transition (E1) the difference is limited to $\Delta J \leq 1$, for an electric quadrupole transition (E2) to $\Delta J \leq 2$, and so on. Although transitions with $\Delta J = 0$ are possible, transitions from a state with $J = 0$ to another with $J = 0$ are not [42]. The transition probability decreases by many orders of magnitude for high-order multipole transitions compared to an E1 transition [42]. So excited states for which a high-order multipole is the only decay mode feature a long lifetime, such as the metastable state in rhenium which can decay only via an E5 transition [16].

In the decay chain of the produced excited states in the EBIT, it is possible that the ion decays to an electronic configuration of a metastable state instead of the ground state. These metastable states can have lifetimes in the order of several hundred days [17], influencing the mass measurements at PENTATRAP. Therefore it is of interest for the future mass-ratio determination of ^{163}Ho and ^{163}Dy to see if metastable states are also present. For this purpose, FAC calculations were carried out for both elements in a charge range of 20+ to 31+ for holmium and 19+ to 30+ for dysprosium. The thereby determined metastable atomic states can be used as a criterion when choosing the charge state suitable for the mass measurements.

A short overview of the electronic structure of HCI is given in section 3.1 and is followed by a brief description of the theoretical models used in the FAC calculations in section 3.2. Finally, section 3.3 summarizes the meta-stable states of holmium and dysprosium predicted by FAC calculations.

3.1 Electronic Structure in HCI

In atoms and ions the electrons are ordered in shells. The shells are characterized by the principle quantum number n, while $n = 1$ denotes the innermost shell. As n increases, the electrons are less strongly bound to the nucleus. The shells contain subshells characterized by the quantum number for the orbital angular momentum l, which ranges from zero to $n - 1$ in each shell. Each subshell is $2(2l + 1)$ degenerate, meaning that it can be filled with this amount of electrons.

In the ground state, the shells are filled with electrons to maximize the binding energy of the electrons in the shells, which corresponds to minimizing the total energy of the system. In atoms and ions with multiple electrons, the electric field an electron experiences is altered due to the presence of other electrons. Additionally, screening of the electric field of the nucleus by inner shell electrons effects the ordering of the atomic shells. In atoms and ions with multiple electrons, the shells are ordered according to the Madelung $n+l$-rule. In the ground state, the shells with the smallest value of $n+l$ are filled first, for equal values the one with the lower n is filled first. For ions with a smaller amount of electrons the influence of the other electrons decreases and the shells are filled according to Coulomb ordering. In this case, the shells with the lowest n are occupied first. The subshells are also filled in ascending order. This is equivalent to the level ordering in hydrogen and hydrogen-like ions. An example of both orderings is given in Equation (3.1).

$$\begin{aligned} &\text{Madelung ordering} = 1s^2 2s^2 2p^6 3s^2 3p^6 4s^2 3d^{10} 4p^6 5s^2 4d^{10} 5p^6 6s^2 4f^{14} ... \\ &\text{Coulomb ordering} = 1s^2 2s^2 2p^6 3s^2 3p^6 3d^{10} 4s^2 4p^6 4d^{10} 4f^{14} 5s^2 ... \end{aligned} \tag{3.1}$$

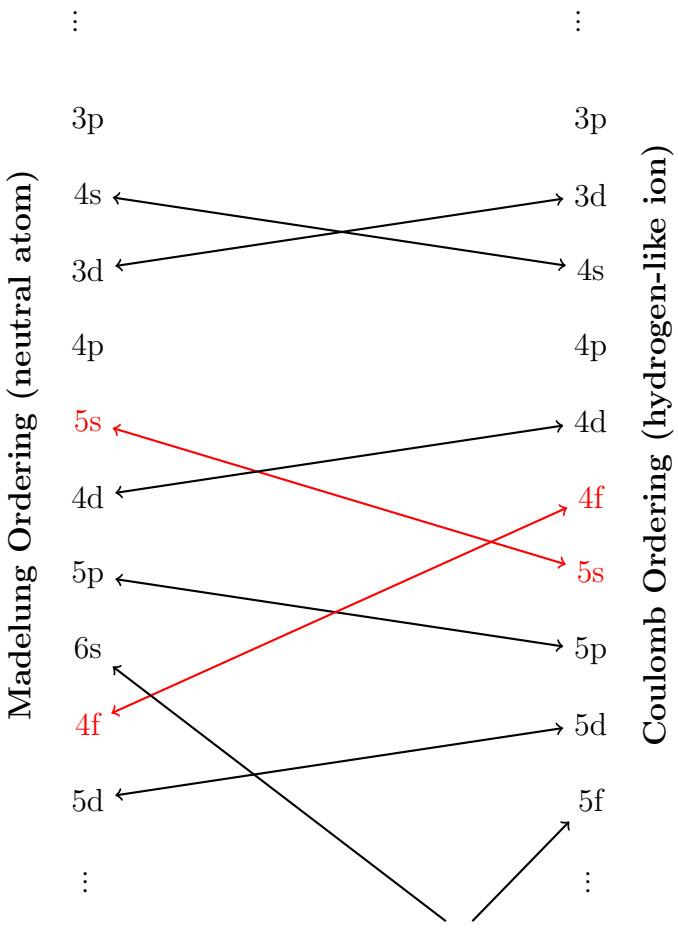

Figure 3.1: Level crossings when going from Madelung to Coulomb ordering. The order of the atomic shells in which the electrons are more strongly bound switches at these crossings. The level crossing 4f−5s, which is especially interesting for holmium and dysprosium in charge states 20+ to 30+, is shown in red. Based on [43].

Here, the first number denotes the principle quantum number n; s, p, d, f corresponds to $l = 0, 1, 2, 3$ and the number in superscript gives the number of electrons in the shell. Depending on the number of electrons, the outermost shell is filled only partially. If only one electron occupies a shell the number is usually omitted.

In an isoelectronic sequence, increasing number of protons but constant number of electrons, a level crossing will occur, from Madelung ordering for the neutral atom to Coulomb ordering for the hydrogen like ion. This is the point at which, for example, the 4f and the 5s shells change the ordering in which the electrons more strongly bound. A comparison of the two orderings and the level crossings is schematically shown in Figure 3.1. Ho^{20+} lies in the isoelectronic sequence of neutral Ag and is the lowest charge state of holmium considered in the FAC calculations. In this sequence the level crossing of the 4f and 5s shells occurs between Pm^{14+} and Sm^{15+} [39]. For Sm^{15+} the outer most electron is bound in the 4f shell, whereas for Pm^{14+} it lies in the 5s shell. Since Ho^{20+} lies further along the sequence, the outermost electron is bound in the 4f shell in the ground state and in Ho^{21+} for the lowest-lying excited state an electron is raised from the 4d to the 4f shell.

3.2 Flexible Atomic Code

The Flexible Atomic Code is a software package by M.F. Gu for the calculation of various atomic properties and processes [44]. It can be used to calculate atomic energy levels, radiative transition rates, collisional excitation and ionization by electron impact, photoionization, autoionization, radiative recombination, and dielectronic capture. In the work of this thesis, FAC was used for the calculation of atomic energy levels and radiative transition rates for the search of meta-stable electronic states in holmium and dysprosium.

The theoretical approach of FAC is relativistic configuration interaction (CI). The Dirac-Coulomb Hamiltonian is used to calculate the energy levels of an ion with N electrons. It is given by:

$$H = \sum_{i=1}^{N} H_{\mathrm{Dirac}}(i) + \sum_{i<j}^{N} \frac{1}{r_{ij}} \ , \tag{3.2}$$

where H_{Dirac} is the single-electron Dirac Hamiltonian for the potential of the nucleus and which accounts for relativistic effects. The second term, $\frac{1}{r_{ij}}$, describes the Coulomb interaction of the electrons with each other. Higher-order QED effects, such as retardation and recoil, are accounted for by adding the Breit interaction, with zero energy limit for the exchanged photon, to the Dirac-Coulomb Hamiltonian. The screened hydrogenic approximation is used for the consideration of self-energy and vacuum polarization [45].

The basis states of this Hamiltonian (Φ_ν), configuration state functions (CSF), are an antisymmetrized product of N one-electron wave functions (Dirac spinors). For these one-electron wave functions a local central potential is assumed for which the screening of the nuclear potential by other electrons is taken into account. The total atomic state function is then given by the sum of these basis states [44]:

$$\Psi = \sum_{\nu} b_\nu \Phi_\nu \ , \tag{3.3}$$

where b_ν are mixing coefficients.

The single multipole approximation was used for the calculation of the radiative transition rates. In this approximation arbitrary multipoles can be calculated but interference between different multipoles is neglected.

According to [45], FAC gives energy levels with an accuracy of a few eV and transition rates with an uncertainty of 10 - 20%, although this can vary if the transitions are not in the x-ray regime. Not all physical processes are treated by the FAC, for example two-photon decay and three-body recombination are neglected. This has an influence especially on the transition rates which is why they cannot be taken as reliable values in general.

3.3 Meta-stable states and suitable charge states for mass measurements

With a precision of the mass-ratio measurements of better than 10^{-11} at PENTATRAP, meta-stable states in the order of 100 eV do not pose a problem, as they can be easily distinguished from the ground state during the data analysis process. Much more problematic are lower lying meta-stable states at several eV excitation energy. A long measurement time is needed to acquire enough statistics to be certain whether the mass-ratio measurement is performed on an excited state or the ground state. In the worst case, the metastable state is not identified which will result in a systematic error for the measured mass ratio. Of course, this also depends on the production probability of the metastable state in the EBIT to which many factor contribute along the decay chain. However, this was not further investigated since there are numerous transitions from higher excited states to all the metastable states obtained in the FAC calculation.

To prevent this from happening, the charge states with which the mass-ratio measurements are carried out should be chosen such that they do not have low-lying metastable states. This is only one criterion in the selection of charge states as also closed atomic shells for easier theoretical calculation of the binding energy of the removed electrons, production rates in the EBITs, a high enough charge state in order to achieve the desired precision and low enough charge exchange rate in the trap vacuum play an important role.

Table 3.1 shows the electronic ground state configurations and their J-values for the holmium and dysprosium charge states for which excited states were calculated. Since the dysprosium nucleus ($Z = 66$) has one proton less than the holmium nucleus ($Z = 67$), both ions have the same amount of electrons and electron configuration at charge states that are shifted by one. The abbreviations used for the electronic configurations are given by:

$$\begin{aligned} [\mathrm{Ar}] &= 1s^2 2s^2 2p^6 3s^2 3p^6 \\ [\mathrm{Kr}] &= 1s^2 2s^2 2p^6 3s^2 3p^6 3d^{10} 4s^2 4p^6 \end{aligned} \tag{3.4}$$

For the future mass ratio determination of ^{163}Ho and ^{163}Dy the excited electronic states were calculated for both elements with the Flexible Atomic Code in the range of 19+ to 30+ for dysprosium and 20+ to 31+ for holmium as this corresponds to the same electron configurations in the ground state. From this data, the metastable states were obtained. An excited state was defined as metastable if its decay rate was lower than $2.8 \cdot 10^{-4}$ 1/s, which corresponds to a lifetime of 1 hour. If the lifetime of a state is shorter than 1 hour it will not influence the mass-ratio measurements, as it decays before enough statistics are acquired in the Penning traps or even before it is loaded. The metastable states of holmium and dysprosium in these charge states are listed in Table 3.2 along with their electron configuration and J-value. The uncertainty of the energy of the states is given as a few eV [45].

The states obtained with the FAC calculation are not all truly meta-stable. For example, it has been shown that magnetic interaction can produce an inversion of states 2^3P_0 and 2^3P_1 in helium-like ions [46]. If close to a level crossing, where the energy separation of two states is small, hyperfine interaction can cause mixing of these

Table 3.1: Ground state electron configurations of holmium and dysprosium for the charge states for which excited states were calculated using FAC. J is the total angular momentum of the bound electrons, derived by coupling of the orbital angular momentum and the electron spins.

charge state Dy	charge state Ho	electron configuration	J
19+	20+	$[Kr]4d^{10}4f^{1}$	5/2
20+	21+	$[Kr]4d^{10}$	0
21+	22+	$[Kr]4d^{9}$	5/2
22+	23+	$[Kr]4d^{8}$	4
23+	24+	$[Kr]4d^{7}$	9/2
24+	25+	$[Kr]4d^{6}$	4
25+	26+	$[Kr]4d^{5}$	5/2
26+	27+	$[Kr]4d^{4}$	0
27+	28+	$[Kr]4d^{3}$	3/2
28+	29+	$[Kr]4d^{2}$	2
29+	30+	$[Kr]4d^{1}$	3/2
30+	31+	[Kr]	0

two state. In this way, the 2^3P_0 state has a finite lifetime and the ground state 2^1S_0 is eventually reached although a direct transition is forbidden by the J selection rules.

A similar effect can be attributed to some of the metastable states calculated by FAC of holmium and dysprosium, for example in Ho^{21+} the excited state $[Kr]4d^{9}4f^{1}$ with $J = 0$ (157.0 eV). Since the ground state and this state both have a total angular momentum of $J = 0$ and the state is the lowest excited state, FAC does not give a decay rate of this state, as this transition is forbidden. However, in reality this state is not metastable due to level mixing [47]. The same holds for the respective state in Dy^{20+}. This and other effects (e.g. two-photon decay, three-body recombination) not taken into account in FAC can considerably shorten the lifetime of the presumably metastable states. For this reason, the lifetimes are not given in Table 3.2. In total it can be said that the state prediction with FAC, electronic configuration and energy, are reliable for the identification of possible metastable states, but the lifetimes are not necessarily reliably calculated by FAC therefore some states are not truly metastable. The atomic shells considered in the calculations are listed in the appendix (chapter 6) for each charge states.

Considering the mass-ratio measurements the charge states Ho^{24+}/Dy^{23+}, Ho^{26+}/Dy^{25+} and Ho^{27+}/Dy^{26+} would be a poor choice as these possibly feature low-lying metastable atomic states. Ho^{23+}/Dy^{22+}, Ho^{25+}/Dy^{24+}, Ho^{28+}/Dy^{27+}, Ho^{29+}/Dy^{28+}, Ho^{30+}/Dy^{29+} on the other hand do not have any such metastable states. For the other charge states investigated, the possible metastable states are energetically far away from the ground state such that mass-ratio measurements are not influenced.

Table 3.2: Metastable atomic states of holmium and dysprosium obtained with FAC. For most excited states the energy of state for Dy and Ho are identical. Whenever they differ both are given, the first value corresponds to the state in Dy the second to Ho. The uncertainty of the energy is a few eV [45]. Excited atomic states were calculated for all charge states from 19+ to 30+ for Dy and 20+ to 31+ for Ho, here only the charge states exhibiting metastable states are listed.

charge state		energy (eV)		electron configuration	J
Dy	Ho	Dy	Ho		
19+	20+	160.9		$[Kr]4d^9 4f^2$	13/2
19+	20+	322.0		$[Kr]4d^8 4f^3$	23/2
20+	21+	157.1	157.0	$[Kr]4d^9 4f^1$	0
20+	21+	162.6	162.4	$[Kr]4d^9 4f^1$	5
20+	21+	325.7	325.5	$[Kr]4d^8 4f^2$	10
21+	22+	161.5		$[Kr]4d^8 4f^1$	13/2
23+	24+	4.4		$[Kr]4d^7$	3/2
25+	26+	11.2		$[Kr]4d^5$	11/2
26+	27+	11.2		$[Kr]4d^4$	4
30+	31+	124.8		$[Ar]3d^{10}4s^2 4p^5\ 4d^1$	0
30+	31+	131.2		$[Ar]3d^{10}4s^2 4p^5\ 4d^1$	3

Chapter 4

Experimental setup of the Tip-EBIT and the Pentatrap experiment

The Tip-EBIT is a Heidelberg compact EBIT (HC-EBIT) [2] in which in-trap laser-induced loading was implemented. It is named after the small wire tip with which the atoms are brought into the trapping region. The new loading technique proved to be very efficient as it allows the production and ejection of HCI of small samples containing as little as 10^{12} atoms (about 0.27 ng). This enables precision measurements on HCI of rare isotopes, such as the mass-measurement of ^{163}Ho at Pentatrap.

This chapter is dedicated to the description of the experimental setup, first of the one used for testing and optimizing the in-trap laser-induced loading in the Tip-EBIT in section 4.1, followed by a detailed description of the laser-injection setup in section 4.2. Finally the Pentatrap experiment presented in section 4.3 to which the Tip-EBIT is connected. This section also includes a brief description of Penning traps and the measurement principle of Pentatrap.

4.1 Setup for optimization of laser-induced loading in the EBIT

In the course of this thesis, the Tip-EBIT with in-trap laser-induced loading was redesigned to the configuration shown in Figure 4.1 and will in the following be referred to as the test setup. The main reason for the redesign was the compatibility with the height of the Pentatrap beamline and easier access to the new laser system. The new features include a new pulsed Nd:YAG laser with a suitable optical setup, a differentially pumped gas injection system and a pulsed drift tube located directly after the EBIT. The description of the components of the test setup will follow the course of the electrons and then the ions. The electrons beam originates at the cathode, passes through the drift tubes in the magnetic structure, and is terminated at the collector. The target injection, the laser setup, the deferentially pumped gas injection, and the x-ray detector are connected to the center of the EBIT. The beamline after the EBIT features a pulsed drift tube, an electrostatic quadrupole lens and a 90° dipole mag-

net for charge-to-mass ratio selection. In the end, the ions are detected in a vacuum chamber housing a Faraday cup (FC) and a microchannel plate detector (MCP) with a phosphor plate. The components will be described in detail in the following.

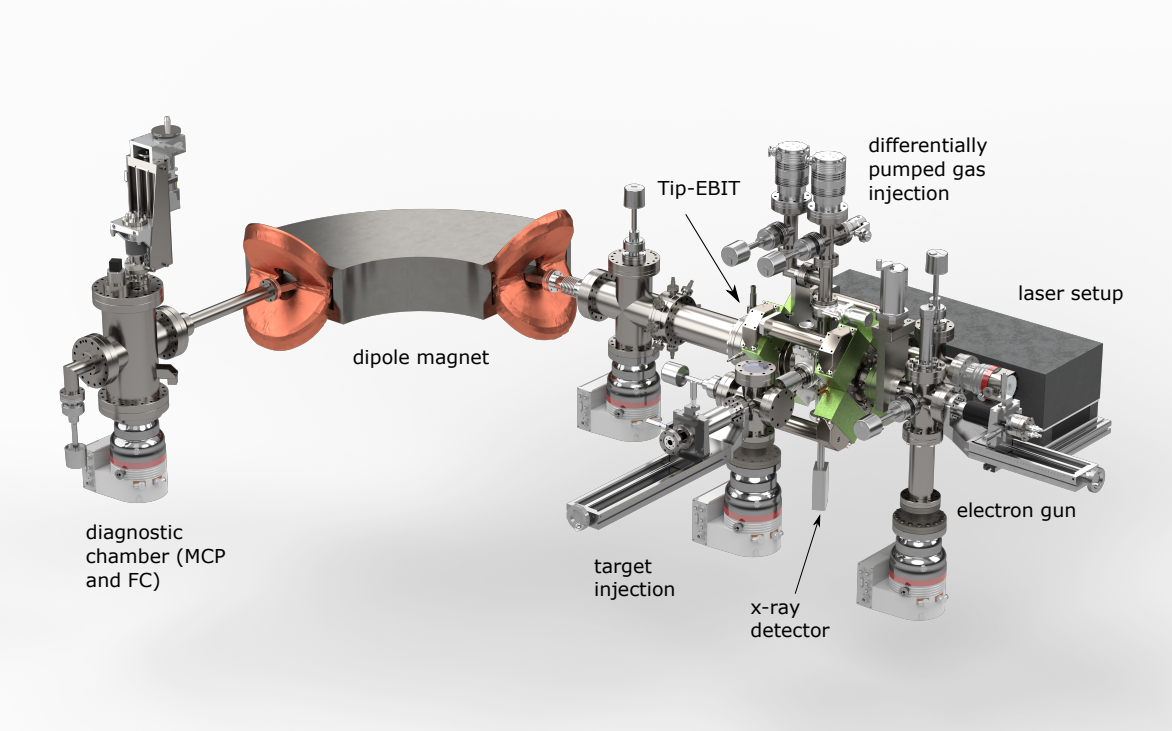

Figure 4.1: Overview of the test setup with the electron gun with its three-axis manipulator on the right side and the Tip-EBIT displayed in green. The 90° dipole magnet and the diagnostic unit are placed on the left side. Attached to the EBIT is the differentially pumped gas injection on top, the target with its three-axis manipulator and the laser setup across from each other to the sides and the x-ray detector attached below.

In the case of this EBIT, the cathode in the electron gun is made out of a porous tungsten matrix uniformly filled with barium oxide [48]. The immediate surrounding gun material is molybdenum which can withstand the hot temperatures (around 1300 K) of the cathode [2]. The low work function of barium allows electrons to be thermally emitted when the cathode is heated. The heating current is typically set to values between 1.2 and 1.3 A. Besides the cathode, the electron gun features a focus electrode and an anode (cf. Figure 4.2). The electrodes are spatially separated and electrically isolated by ceramic rods. The cathode is set to a negative potential of a few kV while a positive voltage of a few hundred volts is applied to the anode, resulting in an acceleration of the emitted electrons away from the cathode. By adjusting the voltage of the anode the current of the electron beam can be regulated. The focus electrode of the electron gun, located between cathode and anode, is set to a negative potential which focuses the electron beam. The value of the focus voltage is typically set slightly lower, a few 100 V, than the cathode voltage.

The electron gun is fixed to a three-axis manipulator allowing the adjustment of its position for optimal transmission of the electron beam through the EBIT. Due to

possible contamination of the electrodes of the gun and growing discharge currents due to metal residue on the ceramic isolators the cathode was placed into a new electron gun in the course of this thesis.

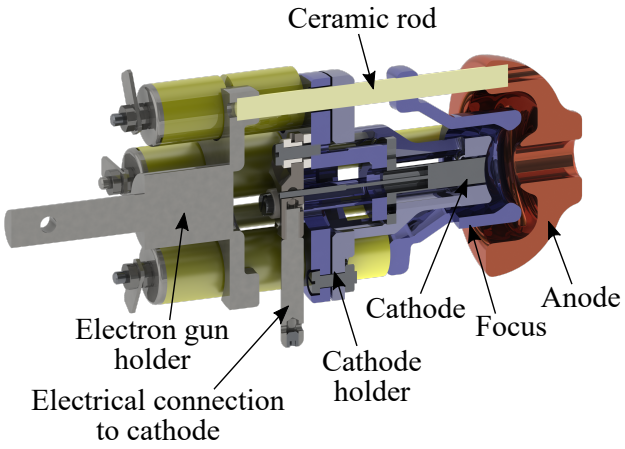

Figure 4.2: Schematic of the electron gun cut in half to show the cathode, the focus electrode, the anode, and the ceramic spacers, adapted from [28].

The stack of drift tubes (DT) in the Tip-EBIT is build up of six trap electrodes threaded on four ceramic rods. Their ordering can be seen in Figure 4.3, where the electron gun is closest to DT1 and the collector is placed after DT5. Typically, the first two drift tubes (DT1 and DT2) are used to focus the electron beam for optimal transmission, DT5 is set to ground and the remaining three form the actual trap with DTC in the center. In contrast to the other closed drift tubes, the central one has four radial slits for mechanical and optical access for, e.g. the laser and the target. To keep the potential distortion due to the slits as low as possible a mesh wire is wrapped around DTC allowing mechanical access only on the side of the target. For a detailed description of the effect of the mesh wire and the one open side for the target on the homogeneity of the potential, see [28]. The fourth drift tube (DT4) is connected to a Behlke high-voltage switch allowing to switch the voltage applied to this electrode from a value higher than the voltage applied to DTC to a lower value in less than 100 ns [49]. When the voltage is switched to a lower value the trap potential is opened axially and the HCI can exit the EBIT towards the collector and the beamline. For typical voltages applied to the drift tubes, see Figure 5.4.

A silicon drift x-ray detector (Ketek GmbH, Vitus H50) is attached to the EBIT close to DTC and picks up the emitted x-rays of the trapped ions, emitted due to the processes described in section 2.2, e.g. radiative recombination. Following these interactions, the x-rays are emitted at energies characteristic for the trapped ion species, for example, they correspond to the specific energy separation of their electronic shells. The spectra obtained with the x-ray detector give insight into whether ions are successfully trapped and which species of ions occur.

After passing the drift tubes, the electron beam continues towards the water-cooled collector. Following the gradient of the magnetic field, the electron beam widens (cf. section 2.1) and hits the collector surface. The current caused by the electrons on the collector is measured by connecting it via an ampere meter to ground. This current can

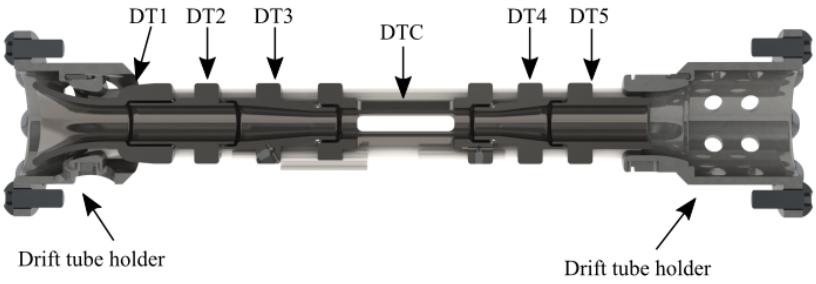

Figure 4.3: A cut through the six drift tubes of the EBIT is depicted. The electron gun would be located to the left of the first drift tube (DT1) and the collector to the right of the fifth (DT5) with the electron beam passing from left to right. The radial slits of the central drift tube are visible. Adapted from [28].

be used to optimize the transmission of the electrons through the EBIT by comparing it to the emission current of the cathode. Following this part of the collector are two electrodes to which a voltage, more negative than the cathode, is applied to prevent any electrons from passing into the beamline.

Previously for gas injection, the fine-dosing valve was installed directly at the main vacuum chamber of the EBIT. Opening the valve introduces a minor leak to the vacuum system which results in a dispersion of the injected gas throughout the main vacuum chamber. As a result, only a small fraction of the injected gas interacts with the electron beam and is ionized. This leads to residual amounts remaining in the EBIT after the valve has been closed, enhancing the background signal. The new, differentially-pumped gas-injection system uses the same fine-dosing valve which is now placed behind two consecutive apertures with a radius of 2-3 mm. The apertures were implemented by using copper disks with a hole of 2-3 mm radius in the center instead of standard copper gaskets. The areas isolated by the apertures are each equipped with a separate turbo molecular vacuum pump and present the stages of the differentially pumped injection system. The setup is displayed in Figure 4.4. With this setup, the gas is injected in the first stage and then proceeds through the first aperture to the second stage and then only after passing the second aperture enters the EBIT as a collimated beam. This way, only a small gas stream reaches the trapping volume and the electron beam so that the background pressure in the EBIT is not notably influenced. When closing the valve, the injected species vanishes after about two trap cycles (≈ 2 s, cf. Figure 5.3) without remaining as additional background gas.

Following the EBIT downstream in the beamline, a pulsed drift tube (PDT) was installed during the work of this thesis. It consists of a stainless steel pipe attached to a CF100 flange. It is connected via a Behlke high-voltage switch and some buffer capacitors to a high-voltage power supply. This allows to change the applied voltage in a range of 10 kV in less than 100 ns [49]. The ions can be pulsed to any required energy independent of the energy with which they are accelerated from the EBIT. The main advantage of the PDT is that now ions can be produced and extracted at arbitrary EBIT potentials without requiring new settings for the focusing and steering further down the beamline if the energy to which they are pulsed is kept constant.

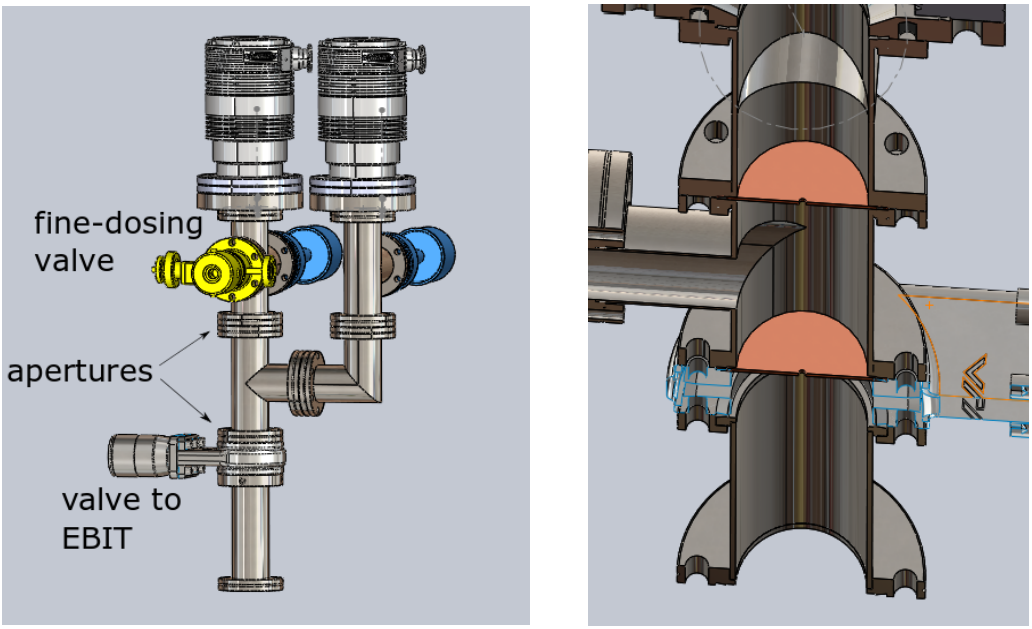

Figure 4.4: Schematic of the new, differentially-pumped gas-injection setup. On the left the full gas-injection setup is displayed as it is attached to the Tip-EBIT. The fine-dosing valve is shown in yellow. The image on the right is a cut through the vacuum chamber making the apertures visible.

This saves a large amount of time when changing EBIT settings, for example changing the potentials of the drift tubes to alter the electron beam energy for the production of certain charge states, especially considering the longer beamline with more focusing elements at the PENTATRAP experiment to which the EBIT is now attached.

Located after the PDT is an electrostatic quadrupole lens for steering and focusing of the ion bunch. The applied voltages are optimized for the best possible transmission through the dipole magnet following downstream and are in the order of 100 V. The dipole magnet forms a 90° bend in the beamline and the current in the coils can be set to adjust the magnetic field the ions are subject to. The degree to which an ion's path is bent due to the magnetic field depends on its charge-to-mass ratio. Therefore, only ions with a specific charge-to-mass ratio will pass the 90° bend at a given magnetic field. This allows a separation of charge states and isotopes. When the magnet current is ramped over a certain range, charge state spectra can be acquired. An example of a charge state spectrum is shown in Figure 4.5. The most abundant peak, at a charge to mass ratio of 0.244 ($^{209}Bi^{51+}$), was fitted with a Gaussian curve, shown in the inset. The full width at half maximum of the Gaussian curve allows a determination of the resolution of the dipole magnet, $\frac{q/m}{\Delta q/m} = 360 \pm 27$.

The last part of the setup located after the dipole magnet is the detection chamber. It contains a microchannel plate detector (MCP) in chevron configuration and an adjacent phosphor screen viewed with a camera and a Faraday cup (FC) connected to an oscilloscope via a charge amplifier (Femto HQA-15M-10T, amplification factor: 10 V/pC). An MCP contains parallel channels tilted with respect to the surface of the plate. In chevron configuration, two consecutive plates are placed so that the angles of their channels are opposite to each other. An incoming charged particle hitting the

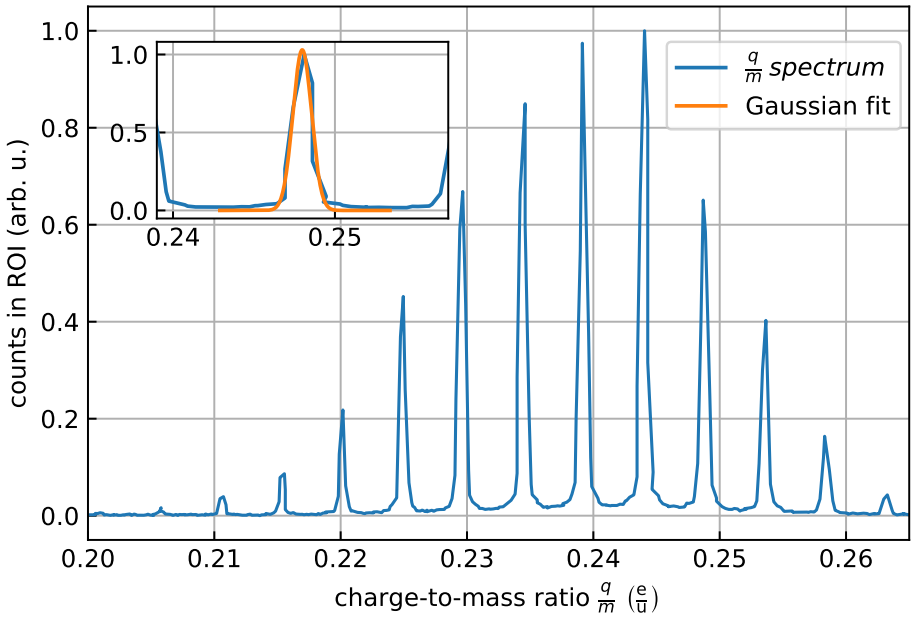

Figure 4.5: This figure shows a very clean charge state spectrum of bismuth. The most abundant charge state is $^{209}Bi^{51+}$ to which a Gaussian curve was fit $\left(f(x) = Ae^{-\frac{(x-x_0)^2}{2\sigma^2}}\right)$, shown in the inset. The fit resulted in the following parameters: $A = 1.030 \pm 0.085$, $x_0 = 0.243990 \pm 0.000022$, and $\sigma = 0.000288 \pm 0.000022$.

wall of a channel will release electrons. A voltage of about 1 kV is applied between the front and back plate to accelerate the electrons towards the back. The accelerated electrons will interact with the channel wall, creating a cascade of electrons. In our setup, the back plate is set to ground and a negative voltage is applied to the front plate which defines the gain of the MCP. When exiting the back plate, the electrons are further accelerated by 3.2 kV towards the phosphor screen creating a fluorescence signal that can be picked up by the camera. The acquisition time of the camera is set to 3 ms to pick up the entire fluorescence time of the phosphor screen. An MCP with a phosphor screen has the advantage of position-sensitive detection. This simplifies the focusing and steering process and also leads to a higher resolution in the charge state spectra. The Faraday cup is used for measurements of absolute ion numbers by measuring the charge due to the HCI colliding in its surface. Considering these aspects, both detection devices are important tools for our measurements.

4.2 Laser-injection setup

In the experimental setup displayed in Figure 4.1 the laser and the target are located on opposite sides of the EBIT, enabling the laser to hit the target surface orthogonally. For laser-induced loading, a short laser pulse of 7 ns is shot onto a target containing the species of interest, to detach atoms from the target surface for ionizing and trapping in the electron beam. To allow this process, the target is moved as close as possible to the electron beam inside the central drift tube. The target is steered by a three-

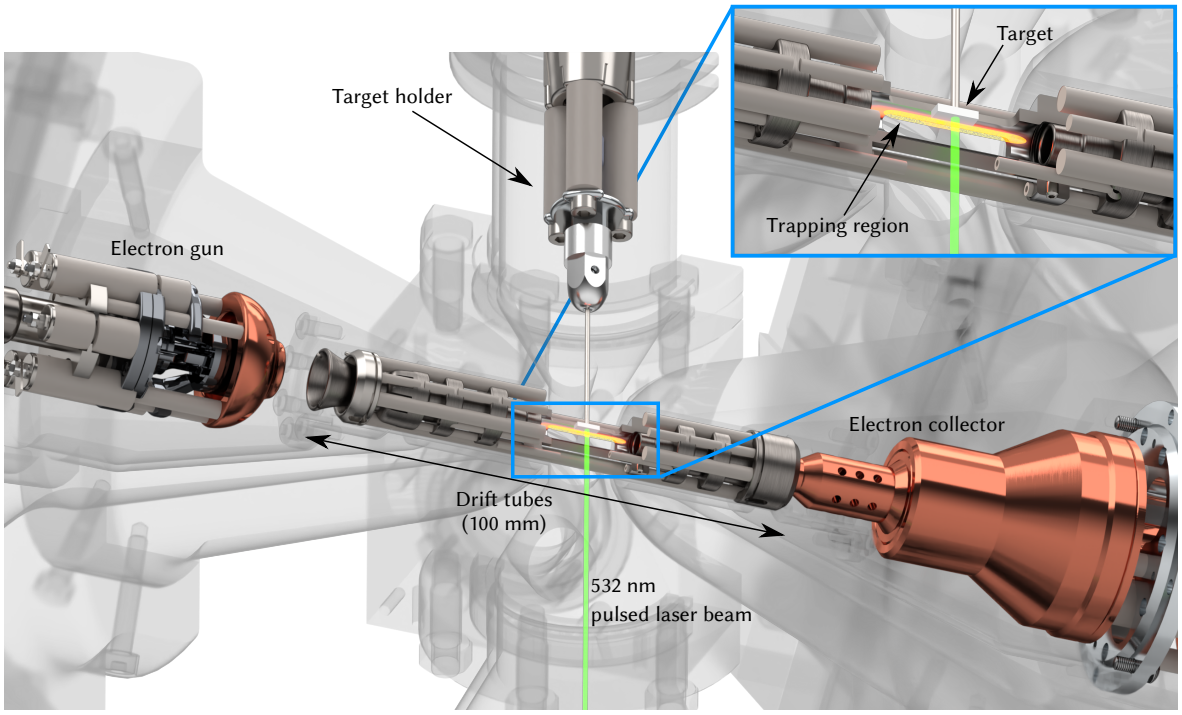

Figure 4.6: Model of the EBIT with the main components and the laser-induced loading viewed from above. To the left is the electron gun followed by the drift tubes in the center with the electron collector to the right. The target is placed inside the central drift tubes with an incident laser pulse, the central drift tube is cut in half for visibility. The inset shows the central drift tube with the target, the laser beam ($\lambda = 532\,\mathrm{nm}$, green) and the trapping region up close. The image is adapted from [50].

axis manipulator with a step motor for each of the three axes. The position of the target relative to the cut out of the wire mesh and the central drift tube is adjusted using a camera located in the laser setup viewing approximately along the propagation direction of the laser beam as indicated in Figure 4.7. The radial distance to the electron beam is optimized by monitoring the x-ray spectrum. When the target is about 20 mm away from the trap center it is set to the same voltage as the central drift tube. As the target is moved in closer a minimum of the counts of the x-ray detector is reached roughly when the target position matches the gap in the central drift tube, filling the potential gap. Moving the target in further will, at some point, result in bremsstrahlung when the target gets too close to the electron beam. This is detectable as a strong increase in the count rate of the x-ray detector. The target is placed in its final position by moving it out by about 100 μm or less to the position closest to the electron beam which is far enough away to not produce bremsstrahlung. When the target is positioned, the applied voltage is adjusted for maximal electron beam transmission, typically some ten volts lower than the voltage applied to DTC.

The target is made out of titanium wire with a diameter of 1 mm. Some target models have additional features such as a thread cut into the wire or a titanium plate attached to it increasing the target surface. The target with the titanium plate is depicted in the inset of Figure 4.6. The material was chosen since titanium is a rather light element so that only low background signal is to be expected when producing

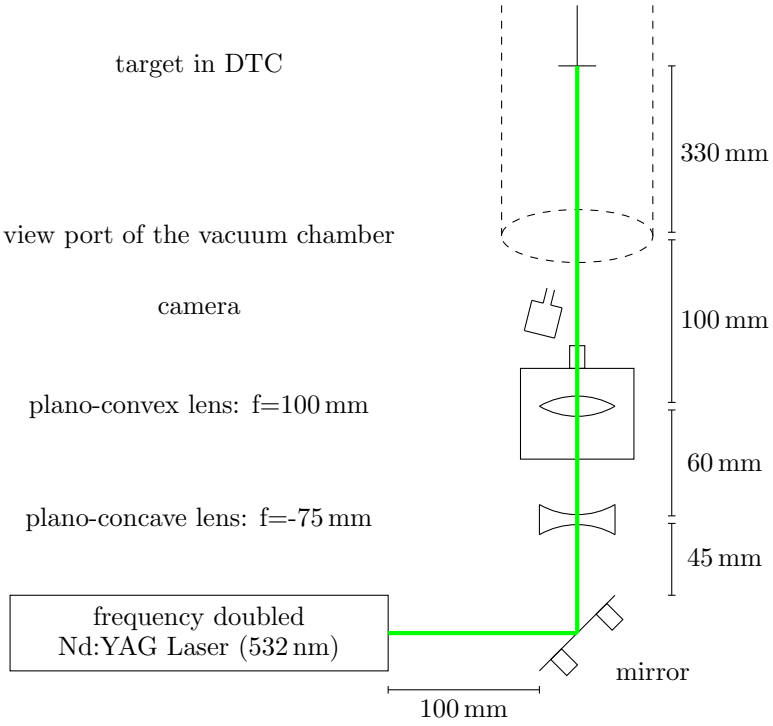

Figure 4.7: Schematic view of the laser setup from above, starting at the Nd:YAG laser and following the laser beam to the target. The mirror has two step motors attached to its holder for shifting the position of the laser spot on the target. The plano-convex lens for focusing of the laser is mounted on a platform so that the distance between the lenses can be changed using a step motor for focusing the laser beam on the target. The image is not to scale with the setup.

heavier ions due to evaporative cooling (cf. section 2.3). Additionally, it had to be vacuum suitable and an electric conductor. For macroscopic sample sizes with an almost infinite number of atoms, the sample material is either placed into a small hole in the titanium plate or, as in the case of ^{165}Ho, which is available as a foil, it is spot welded onto the surface. The targets with small sample sizes are prepared using the "Drop-on-Demand" ink-jet printing technique [51] for which a diluted solution of the sample is printed on the titanium surface. For holmium, a nitrate solution is used. The volume of a drop is in the order of a few nL, resulting in the target material covering only a fraction of the target surface. The sample material is not visible without magnification. The number of atoms can be chosen as needed by dilution with an uncertainty of about 5%. Targets in the range of $10^{10} - 10^{16}$ atoms were made and tested in this setup.

When exchanging the target, the manipulator is set so that the target is pulled out of the EBIT to the left as far as possible. A valve is closed, isolating the chamber containing the target from the EBIT and the rest of the experiment. The small volume containing the target is then vented and by removing two flanges, the target can be taken out and replaced by a new one. Once the vacuum chamber is closed and pumped to a pressure corresponding to the EBIT the valve is opened and the new target can be inserted into the central drift tube following the procedure described above. The

exchange of the target can be accomplished in about 30 min with an additional several hours waiting time for suitable vacuum pressure.

The laser in our setup is a compact pulsed Nd:YAG laser (Litron Lasers Nano S 30-50) with a maximal energy output of 30 mJ at a wavelength of 1064 nm. After passing through an attenuator it is frequency-doubled to 532 nm with a maximal energy of 15 mJ. The attenuator allows to adjust the energy output of the 532 mJ pulses. In addition, the housing for the frequency doubling contains a laser pointer for alignment. The setup for focusing the laser beam onto the target is shown in Figure 4.7. The laser pulse is reflected by 90° by a silver-coated fused silica mirror (Thorlabs PF10-03-P01) after which it passes through two lenses. The lenses are both UV fused silica lenses with anti-reflective coating. The first one is plano-concave with a focal length of -75 mm while the second one is plano-convex with a focal length of 100 mm (both Thorlabs LC4513-A and LA4380-A). The lens configuration was chosen due to the desired position of the beam waist at the target and due to the longer Rayleigh length when defocusing before a convex lens, compared to a single lens with a focal length of 100 mm. The Rayleigh length describes the distance from the beam waist where the beam radius has increased by a factor of $\sqrt{2}$. A single lens with a focal length of 400 mm would result in the minimal beam waist at the target but with a beam radius larger by a factor of more than 2. The required focal lengths and the positioning were calculated using a Gaussian beam propagation and resulted in an optimal distance of 60 mm for the two lenses. After the lenses, the laser beam passes through a viewport into the vacuum setup. It then crosses the wire mesh covering the slit of the central drift tube and hits the target inserted from the opposite side.

In addition, a camera is located in front of the vacuum view port used for the adjustment of the target and laser spot positions. For this purpose, the mirror is mounted with two step motors so that its angle can be shifted causing the laser spot to move on the target surface. This is used to scan the target surface with the laser to find the printed drop of the target material. Another step motor drives the platform on which the plano-convex lens is fixed. As a result, the distance between the two lenses is adjustable which shifts the focal point of the laser beam. This is useful to fine-tune for the greatest focusing on the target surface.

4.3 The Pentatrap experiment

The Pentatrap experiment is a high-precision Penning-trap mass spectrometer aiming at relative mass uncertainties of 10^{-12} [14]. To reach this so far unprecedented precision it features a stack of five cylindrical Penning traps and uses highly charged ions in the measurements [14]. The full setup is depicted in Figure 4.10. So far a Dresden EBIT (DREEBIT GmbH) was the only source of HCI available at the beamline. With this source only elements that are gaseous or available as volatile organic compounds could be used for mass measurements, as there is no other loading mechanism available for this EBIT. With the addition of the Tip-EBIT with its in trap laser-induced loading the variety of HCI available for mass measurements has been expanded. This will allow the production and subsequently loading of the Penning traps with HCI of rare isotopes such as ^{163}Ho. The measurement of the mass-ratio of ^{163}Ho and ^{163}Dy will contribute to the ECHo collaboration aiming to determine the

electron neutrino mass on the sub-eV level [52]. Before describing the details of the experimental setup of PENTATRAP in subsection 4.3.2, a short overview of the basic principles of Penning-trap mass spectrometry and the measurement scheme using a stack of 5 of Penning traps is given in subsection 4.3.1.

4.3.1 Penning traps and measurement scheme

In a Penning trap, three-dimensional confinement is achieved by a strong homogeneous magnetic field pointing along the trap axis providing radial confinement and a static electric quadrupolar field for the axial confinement. This is shown schematically in Figure 4.8a for a trap with cylindrical electrodes. The magnetic field is generated using a superconducting solenoid surrounding the trap electrodes, while the electric potential is produced by applying suitable voltages to the trap electrodes. Charged particles in a magnetic field are subject to the Lorentz force and thus follow a circular orbit. The orbital frequency is the free cyclotron frequency ω_c that depends on the mass m, the charge q and the magnetic field B in the following way:

$$\omega_c = \frac{q}{m} B \, . \tag{4.1}$$

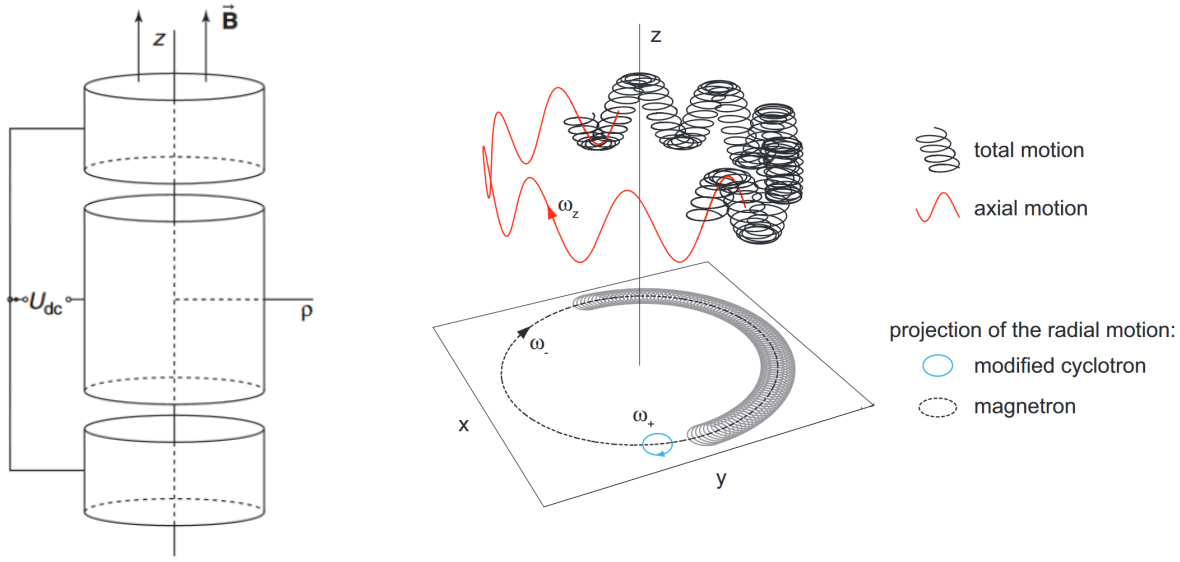

(a) **(b)**

Figure 4.8: A schematic of a cylindrical Penning trap with the magnetic field along the trap axis and the potential U_{dc} applied to the electrodes for axial trapping is shown in **(a)**, taken from [53]. **(b)** depicts the motion of a charged particle in a Penning trap with the three eigenfrequencies shown separately and superimposed, taken from [54].

Due to the superposition of the magnetic and electric field, the motion of a confined particle is altered compared to the free cyclotron motion. The resulting eigenmotions and their superposition are depicted in Figure 4.8b. The three eigenfrequencies are the modified cyclotron frequency (ω_+), the magnetron frequency (ω_-) and the axial frequency (ω_z), given by [53]:

$$\omega_+ = \frac{\omega_c}{2} + \sqrt{\frac{\omega_c^2}{4} - \frac{\omega_z^2}{2}} \tag{4.2}$$

$$\omega_- = \frac{\omega_c}{2} - \sqrt{\frac{\omega_c^2}{4} - \frac{\omega_z^2}{2}} \tag{4.3}$$

$$\omega_z = \sqrt{\frac{2qU_{\mathrm{dc}}}{md^2}} \ . \tag{4.4}$$

Here, U_{dc} is the voltage applied to the central electrode as shown in Figure 4.8a such that a quadrupolar electric field is generated. d describes the geometry of the trap: $d = \frac{1}{2}(z_0^2 + \frac{r_0^2}{2})$, where z_0 is the closest distance between the end electrodes and r_0 is the inner diameter of the central electrode. After all three eigenfrequencies are determined, the free-space cyclotron frequency (ω_c) can be calculated using the Brown-Gabrielse invariance theorem [55]:

$$\omega_c^2 = \omega_+^2 + \omega_-^2 + \omega_z^2 \ . \tag{4.5}$$

At Pentatrap, the eigenfrequencies are measured non-destructively by the image-current detection technique [56]. Figure 4.9 shows a measurement scheme utilizing all the traps. The ion frequencies are measured in traps 2 and 3 simultaneously after loading an ion m_1 and two identical ions m_2 in traps 1-3 as shown in the top part of Figure 4.9. The ions are then adiabatically shifted to trap 2-4 and the frequencies are measured in traps 2 and 3 again. They are then shifted back to the initial position and the measurement is repeated. By following this measurement scheme systematic uncertainties such as magnetic field drift can be reduced, enabling high precision in the mass measurements using the multi-trap configuration [14].

4.3.2 Full setup with the new EBIT

The full Pentatrap setup with the two EBITs as ion sources is displayed in Figure 4.10, along with the beamline and the magnet containing the Penning traps. In the course of this thesis, the Tip-EBIT was attached to the Pentatrap beamline as a source for HCI of rare species.

The Tip-EBIT was attached to the Pentatrap beamline via an electrostatic quadrupole bender which allows switching between ions produced in the DreEBIT and in the Tip-EBIT. When no voltage is applied it will let the HCI of the DreEBIT pass freely towards the 90° dipole magnet. When it is set to high voltage in the range of a few kV it will deflect the HCI bunch of the Tip EBIT changing their course according to the value of the set voltage. The setting should be such that the ions course is bent by 90° allowing a straight path towards the dipole magnet. The first diagnostic unit is placed straight ahead of the Tip EBIT behind the electrostatic quadrupole bender and is equipped with an MCP and phosphor plate. This way, the EBIT settings and the PDT can be adjusted to achieve a maximized output while the electrostatic quadrupole bender is set to ground.

Following the electrostatic quadrupole bender is an einzellens, for which the central electrode is split in four, used for focusing and steering of the ions. The next diagnostic unit is located behind the lens and can be inserted into the beamline from above at two

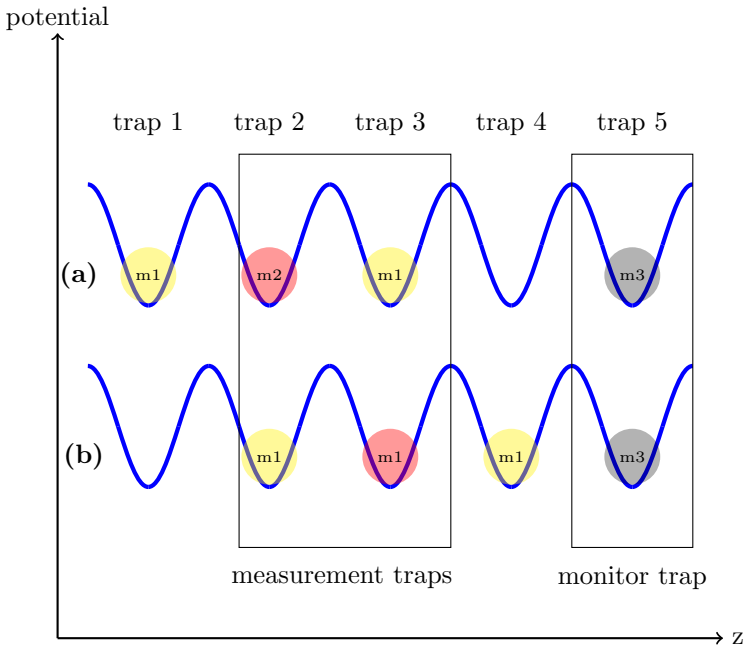

Figure 4.9: Measurement scheme for high-precision mass determination using the stack of five cylindrical Penning traps at PENTATRAP. The blue line indicates the potential wells of the traps. The ions are loaded in configuration **(a)** and the frequencies are determined in traps 2 and 3, after which the ions are adiabatically shifted to the configuration **(b)**. Again, the frequencies are measured in traps 2 and 3 after which the ions are shifted back to the initial configuration. This is repeated several times.

possible vertical positions, one with a FC and the other with an MCP and phosphor plate. The position of the diagnostic unit allows for optimization of the voltage of the electrostatic quadrupole bender to achieve best possible transmission through the dipole magnet which follows afterwards. The dipole magnet forms a 90° bend in the beamline and is used to separate the ions by their charge-to-mass ratio depending on the strength of the magnetic field set by the current in the coils of the magnet.

Following the dipole magnet are another split einzellens, an electrostatic quadrupole bender and an MCP with a phosphor screen in the horizontal part of the beamline. Since the dipole magnet splits the ions by charge-to-mass ratio, the MCP can be used to acquire charge state spectra as with the test setup described in section 4.1 as long as the adjacent electrostatic bender is set to ground. This enables the identification of elements, isotopes and charge states. When a suitable voltage is applied to the electrostatic quadrupole bender, the ions are deflected downwards to the Penning traps. On their way towards the Penning traps, the ions pass another diagnostic unit that can be placed in the ion beam to optimize the voltage of the bender. Two pulsed drift tubes located after it are used to decelerate the ions to an energy at which they can be trapped (around 10 eV). If the pulsed drift tubes are set accordingly, the ions enter the traps and are confined.

Along with moving the Tip-EBIT to the PENTATRAP beamline the pre-vacuum setup of the Tip-EBIT was revised. Previously, each turbo molecular pump was attached to its own pre-vacuum pump (scroll pumps) with a pre-vacuum of about

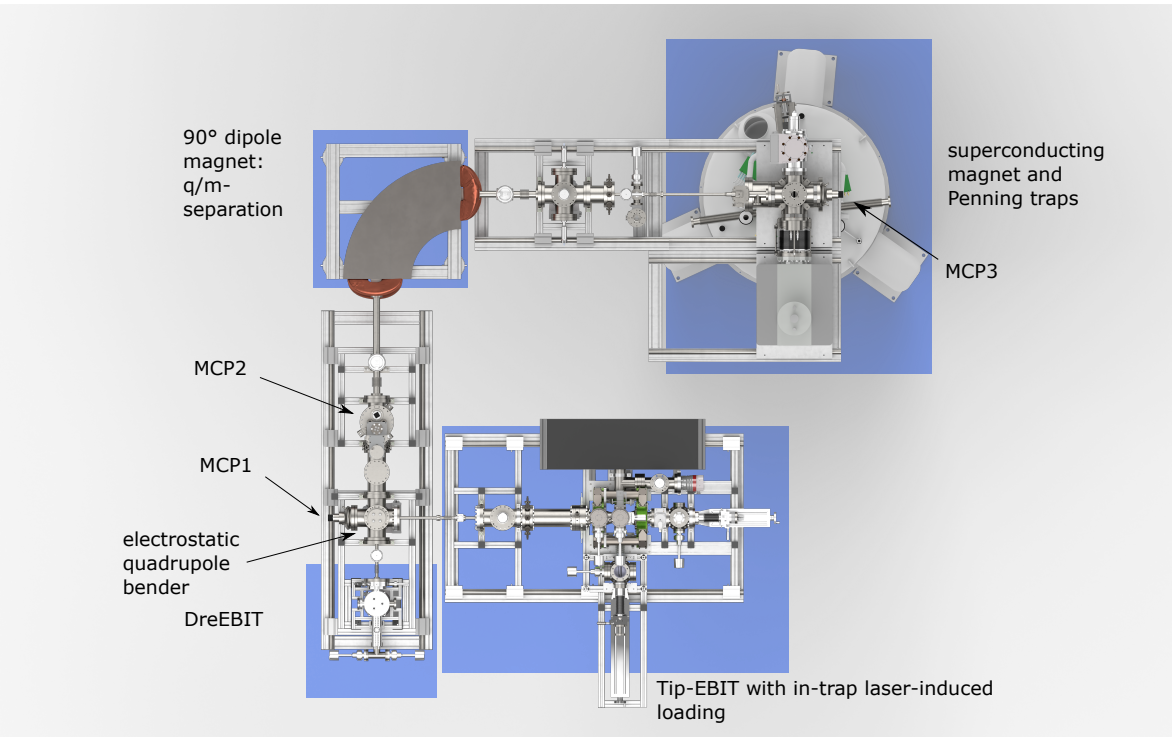

Figure 4.10: Overview of the PENTATRAP experiment with the ion sources, the beamline and the magnet containing the Penning traps below. The Tip-EBIT and the DreEBIT are located at an angle of 90° to each other and are the starting points of the beamline, followed by a 90° dipole magnet, the second part of the horizontal beamline and the vertical part leading to the traps.

10^{-2} mbar. Now all turbo molecular pumps are attached to one turbo molecular pump providing a strongly improved pre-vacuum of $4 \cdot 10^{-6}$ mbar, the pre-vacuum for which is supplied by a single scroll pump providing $4 \cdot 10^{-3}$ mbar.

Chapter 5

Results

In this chapter, the results of in-trap laser-induced loading in the Tip-EBIT are presented. This technique proved to be highly efficient for the production of HCI from small sample sizes containing only 10^{12} atoms. Despite the small sample sizes the targets could be used for several thousand laser shots, producing millions of HCI of the injected species. The first tests were carried out with ^{165}Ho but the procedure was also successfully applied to other elements. Due to the positive results the Tip-EBIT was attached to the PENTATRAP experiment to serve as a source of HCI of rare isotopes for high-precision mass measurements, for example of ^{163}Ho.

In section 5.1 the optimization of the laser-induced loading is discussed, after which section 5.2 focuses on the results obtained with the test setup described in section 4.1. This includes charge state spectra and lifetime and efficiency measurements of samples containing only 10^{12} atoms of ^{165}Ho. The attachment of the Tip-EBIT to the PENTATRAP beamline and the subsequent commissioning is outlined in section 5.3. Finally, section 5.4 describes difficulties concerning the Tip-EBIT and approaches to overcomes them.

5.1 Laser-induced loading

In this section, different target types that were tested for the in-trap laser-induced loading technique are presented. Furthermore, the physical process leading to the laser-induced loading will be discussed. The placement of the targets in the EBIT and the laser setup are described in section 4.2.

Figure 5.1 shows camera images of the target types tested in the EBIT. The two types mostly used are a holmium foil (^{165}Ho) spot-welded onto a titanium plate with a surface of 5 mm^2, in the following referred to as the macroscopic holmium target and a titanium wire with a diameter of 1 mm. A small amount of sample material, varying from 10^{10} to 10^{16} atoms, is placed on the surface of the titanium wire using the Drop-on-Demand 'inkjet' printing technique [51]. The other two target types were also successfully tested, namely a titanium target, of a similar size as the macroscopic holmium target, with two holes that can be filled with sample material and the same titanium wire as the microscopic holmium target but with a thread cut in it and an aluminum collimator shell screwed onto the thread (cf. Figure 5.1). The first of which is useful when working with large quantities of sample material and for fast consecutive

loading of two different species into the EBIT. This can be accomplished by switching the laser position on the target from one sample to the other. The target with the thread was developed with the purpose of the aluminum shell collimating the atoms released due to the laser impact towards the electron beam, increasing the loading efficiency.

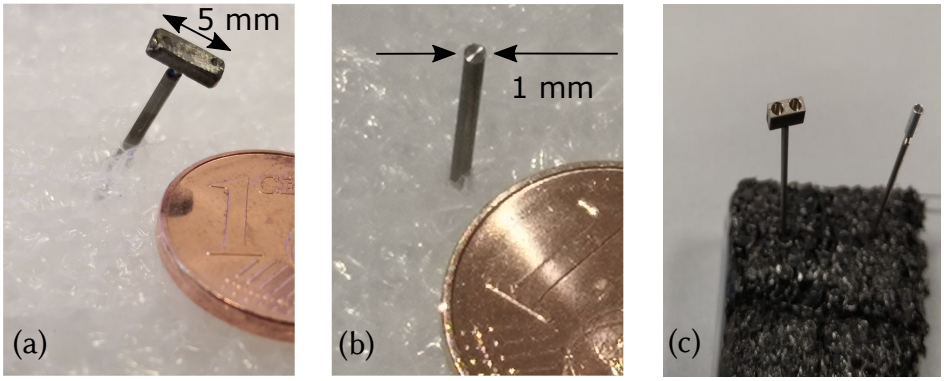

Figure 5.1: Pictures of the different target types used in the Tip-EBIT with a one Euro-cent piece as a size reference. **(a)**: Macroscopic holmium target on which the spot welding marks are visible; **(b)**: A target with 10^{12} atoms of ^{165}Ho printed on the surface of a 1 mm titanium wire. These two target types are the ones mainly used. **(c)**: Pictures of targets which were also successfully tested, first (on the left) a target which has two holes into which sample material can be placed when working with large quantities. Second (on the right) a 1 mm titanium wire with a thread cut in it and an aluminum collimator screwed on top.

As the target types were tested and the loading technique was optimized, the lifetime of the small sample sizes proved to be greater than expected, when assuming laser ablation to be the process with which atoms are detached from the target surface. The lifetime of a target is defined as the number of laser shots for which the sample on the target can be loaded into the Tip-EBIT. To analyze the process happening in the EBIT due to the laser impinging on the target, the average energy transfer per atom for one laser shot was estimated. It is important to note that this estimation only very roughly describes the processes occurring during the injection in the EBIT and the values obtained are to be considered as an order of magnitude estimation only. First the fraction of the laser power absorbed by the target is estimated by considering the reflectivity of the mirror ($R_{\text{mirror}} = 0.86$), lenses (R_{lens}=0.004)[1], the viewport of the vacuum ($R_{\text{window}} = 0.07$)[2] and the titanium surface of the target ($R_{\text{target}} = 0.57501$ [57]), overall resulting in 34% of the initial laser power entering the target. For example, at a typical laser pulse energy of 2 mJ the target absorbs 680 μJ. The size of the laser spot is estimated to have a radius of $r_{\text{laser}} = 300\,\mu$m, judging by the microscope images of the holmium target with a small sample size after use (Figure 5.2). The depth to which the laser penetrates (d) can be described by the law of Lambert-Beer:

$$d = \frac{\lambda}{4\pi\Im(n)} \,, \tag{5.1}$$

[1] values stated by Thorlabs
[2] value stated by vab vakuum

where λ is the wavelength of the laser and $\Im(n)$ is the imaginary part of the refraction index, the extinction coefficient ($k = 3.3511$ [57]), of titanium. In total this gives a volume of $3630\,\mu\text{m}^3$ in which the laser pulse energy is deposited. Using the density of titanium at 20 °C, $\rho_{\text{Ti}} = 4.5\,\text{g/cm}^3$, and the atomic mass $M_{\text{Ti}} = 47.867\,\text{u}$ [58], the number of titanium atoms interacting with the laser pulse is about $2.1 \cdot 10^{14}$. This results in $3.11 \cdot 10^{-18}\,\text{J/atom} = 19.35\,\text{eV/atom}$. Additionally, not all the deposited energy is available for the atoms to escape the target, as part of it is transferred away by the heat conduction of the target material.

The comparatively low energy per atom and the long lifetime of the targets led to the assumption that it is not laser ablation which occurs when the laser hits the target. In the process of laser ablation, the atoms sputtered from the surface would form a plume expanding perpendicular and parallel to the target surface, so that only a small fraction would interact with the electron beam and be ionized [59]. Thus the efficiency would be low and the lifetime of a target containing only a small sample size would be shorter than what was measured (subsection 5.2.2).

To further understand the process happening in the EBIT due to the laser impinging on the target, the surfaces of a selection of targets were investigated using a scanning electron microscope (SEM) with an electron energy of 30 kV and an optical microscope both with a maximal magnification of 2000.

For this purpose, an empty titanium wire, a wire with holmium printed on the surface and other targets used in the EBIT, including the macroscopic one were analyzed. The images obtained with both microscopes are displayed in Figure 5.2. The difference between the empty target (Figure 5.2a) and the one with 10^{16} holmium atoms, which were printed using a nitrate solution, (Figure 5.2b) is visible by the crystal structure on the target. It is also visible that the crystal structure is located not only on the surface but continues in the thread. This is not desirable as the material in the thread is lost for loading of holmium in the EBIT and decreases the overall efficiency. Following this realization, the threaded target design was discarded. However, this might not be a problem for smaller sample sizes, because less solution is applied to the target so it might not spread as far. When comparing the used target (Figure 5.2c) with the unused one (Figure 5.2b) it can be seen that the crystal structure on the surface is gone and instead the entire surface seems to be melted. The melted structure and the fact that there is no crater, as would be expected for laser ablation, indicates a heating process in the laser-target interaction. This implies that the laser-target interaction is due to melting and evaporation of the sample material. Following this investigation, the interaction is referred to as in-trap laser desorption.

In Figure 5.2d the top picture shows that the depth of the holmium foil is much greater than the depth the laser penetrates, giving an almost infinite sample size. The thickness of the foil is indicated in red and the laser spots on the target make up the lighter area in the center.

5.2 Results obtained with the test setup

The measurements presented in this section were carried out using the test setup described in section 4.1. The EBIT is operated in cycles to extract individual bunches of HCI. Figure 5.3 shows a typical trap cycle with the time spans for loading ions via

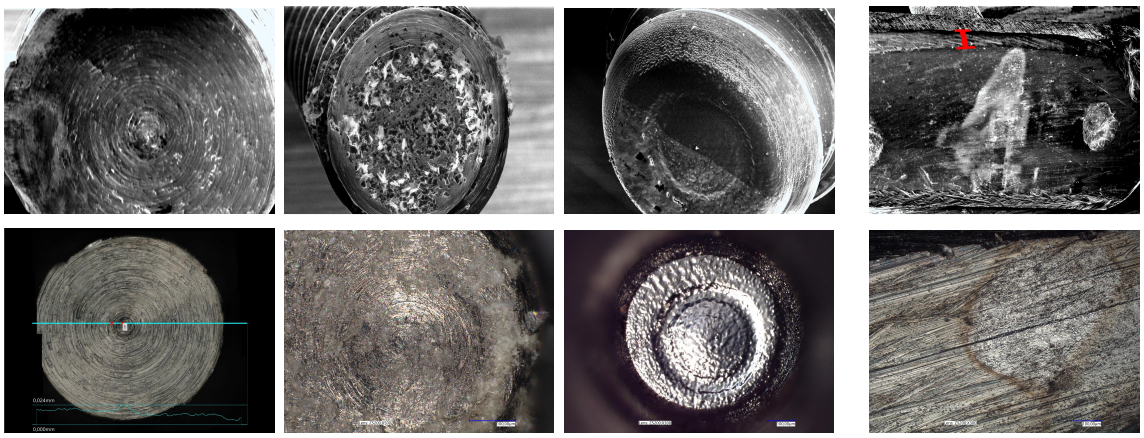

(a) **(b)** **(c)** **(d)**

Figure 5.2: Microscope images of the targets before and after several thousand laser shots. **Top:** Images acquired using an SEM with an electron energy of 30 kV; **bottom:** Images acquired with an optical microscope. The three stages of the targets are shown from left to right: first **(a)** an empty target, then **(b)** one with 10^{16} holmium atoms and the third **(c)** is a target after laser impact. The fourth picture on the far right **(d)** shows the surface of the macroscopic holmium target made from holmium foil. The thickness of the holmium foil is indicated in red, the laser spot is the lighter area in the center and the spot welding points are visible as the round holes on the sides.

laser pulse ($t_{\text{laser}} = 7\,\text{ns}$), keeping the trap closed for charge breeding ($t_{\text{br}} = 1\,\text{s}$), and finally ejecting the ions ($t_{\text{ejec}} = 5\,\mu\text{s}$). The duration of the laser pulse is not variable and the ejection time was kept constant for all measurements. The charge breeding time, on the other hand, was varied for some ion species to influence the charge state distribution.

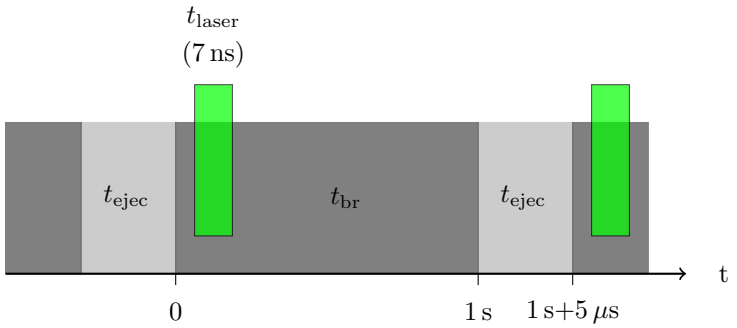

Figure 5.3: Schematic time sequence of the trap cycle in a holmium measurement. The time blocks are not to scale. The duration of each part is given in the image.

Typically measurements were carried out at an electron beam energy of 5.9 keV and an axial trap depth of 50 V. Figure 5.4 shows an example of typical voltage settings for the measurements presented in this section. Depending on the measurement some voltages may vary, especially for the first two drift tubes and the lower value of the fourth one, as these are set for focusing and steering of the electron beam and the ejected ions, respectively.

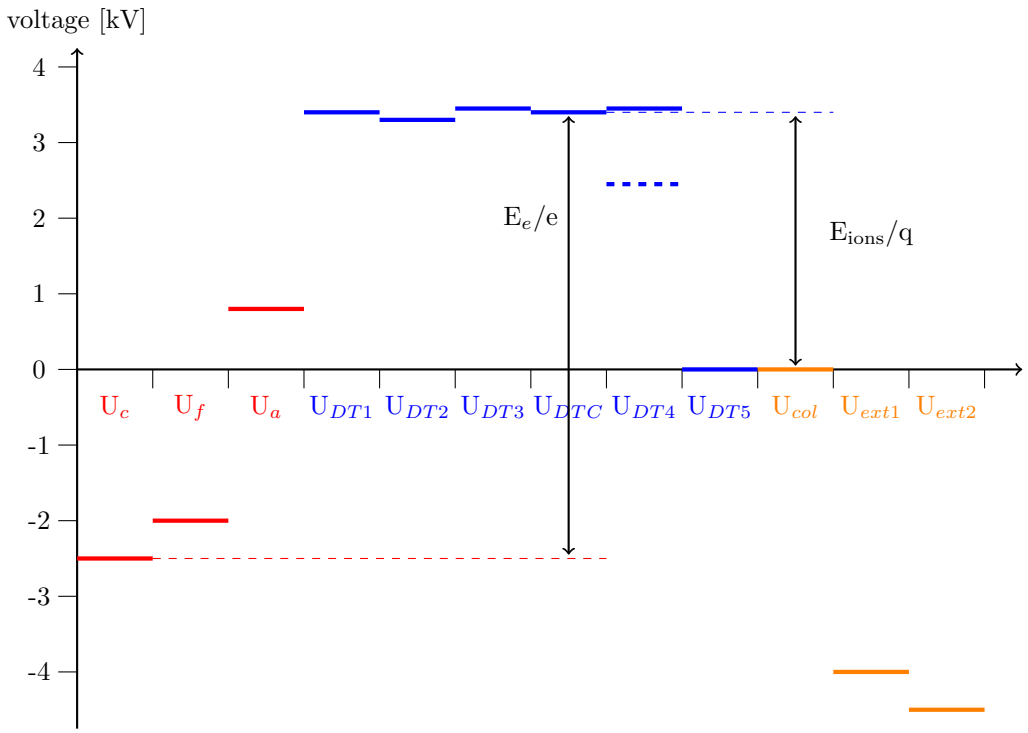

Figure 5.4: Typical voltages applied to the electrodes in the EBIT. The components of the electron gun are shown in red, the drift tubes in blue and the collector in orange. The thick dashed line at the fourth drift tube shows the voltage to which the electrode is switched down for the ejection of the ions. The energy of the electron beam and the ejected ions is defined by the voltage difference of the cathode to the central drift tube and the central drift tube to ground, respectively. The trapping region is formed by the potential well at the central drift tube (DTC).

For ion detection either a Faraday cup (FC) connected to an oscilloscope via a charge amplifier (Femto HQA-15M-10T, amplification factor: 10 V/pC) is used or an MCP. The gain of the MCP is adjusted to reach a strong signal without saturation. The fluorescence signal of the phosphor screen following the MCP is captured with a camera. It is triggered so that the acquisition time starts when the ion bunch hits the MCP. When measuring with the MCP, ten camera frames are averaged and then a circular region of interest (ROI) with a radius of 10 pixels is cut out and summed over to determine the signal strength. The position of the region of interest is placed more or less in the center of the MCP, the exact location is adjusted to overlap with the area in which the ion signal is strongest. Typically the ions are focused so that their image on the MCP resembles a vertical line, which improves the resolution of the charge state spectra compared to a circular signal. When measuring with the FC on the other hand the ions are focused to form a circular signal so that all the ions hit the FC. For these measurements, ten traces of the oscilloscope are averaged, again triggered so that each trace corresponds to an ion bunch. In both cases, the averaging of ten data points is carried out to reduce shot-to-shot fluctuations.

Additionally, the x-ray detector attached to the EBIT, which gives non-destructive feedback of the processes in the trapping region, can be used to detect photon emission

at energies characteristic for certain ion species, showing for example whether holmium is loaded into the trap (cf. Figure 5.5).

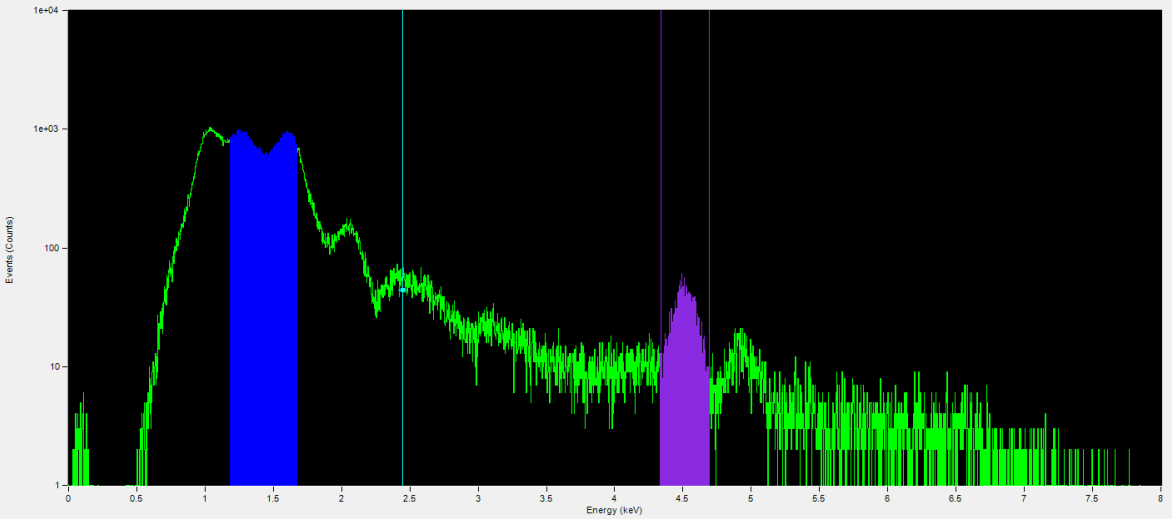

Figure 5.5: Example of the x-ray spectrum while the laser impinges on a holmium target. The holmium peaks are visible in the blue area. The purple area shows a titanium peak used for calibration of the energy on the x-axis.

5.2.1 Calibration

To distinguish HCI of different elements and their charge states, the ion bunch was sent through a dipole magnet with an adjustable current (cf. section 4.1). The ions trajectories are bent according to their charge-to-mass ratio. To determine which elements and which charge states were deflected onto the MCP at a given magnet current, a calibration was carried out. Xenon was chosen for the calibration as it is readily available as a gas and can easily be injected and ionized in the Tip-EBIT. Another criterion fulfilled by xenon is the abundance of several isotopes. This is crucial for the calibration as it causes overlaps in the detected peaks when the charge-to-mass ratios of two isotopes in adjacent charge states equal within the resolution of the dipole magnet:

$$\frac{q}{m_1} = \frac{q+1}{m_2} \,. \tag{5.2}$$

Since the ratios of isotope abundances are known one can associate the measured peak heights to their respective isotopes. The isotope abundances in natural xenon gas are shown in Figure 5.6. When an overlap is found in the spectrum, the charge state follows from Equation (5.2):

$$q = \frac{m_1}{m_2 - m_1} \,, \tag{5.3}$$

for which $m_2 - m_1$ is always greater than 0 due to the initial assumption that isotope 2 is in charge state q+1, so m_2 has to be larger than m_1 for the isotopes to have the same charge-to-mass ratio.

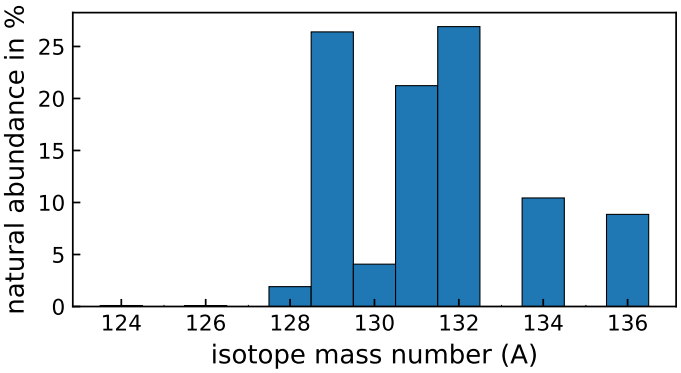

Figure 5.6: Isotope abundances in natural xenon gas, data taken from [58]. As can be seen the isotopes ^{129}Xe, ^{131}Xe and ^{132}Xe are the most abundant with about $20-25\,\%$.

A typical xenon spectrum is shown in Figure 5.7. To achieve the same charge-to-mass ratio range as for the following holmium measurement and to make isotope overlaps well visible, the charge breeding time for xenon spectra was typically reduced to 100 ms. Xenon gas was injected via the differentially pumped gas injection system displayed in Figure 4.4. The isotope structure is visible in the spectrum by the high peak of ^{129}Xe followed by a low one with two adjacent large peaks of isotopes ^{131}Xe and ^{132}Xe, along increasing magnetic field strength. Once an overlap is identified as in the exemplary spectrum at charge states 26+ and 27+ of the isotopes 129-134 and 131-136, a value for the charge-to-mass ratio can be attributed to all the other peaks by counting charge states starting at the overlap. The charge-to-mass ratios and the peak positions in magnetic field units were then plotted and fitted to derive a calibration equation.

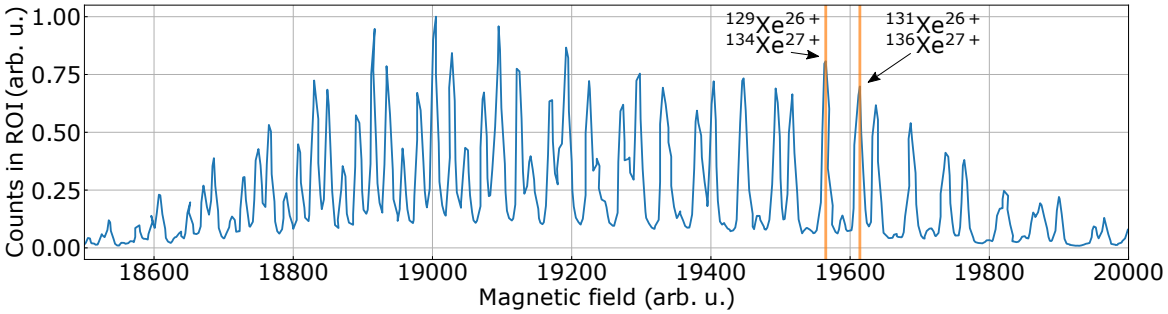

Figure 5.7: Typical uncalibrated charge-to-mass ratio spectrum of xenon for which the isotope overlaps are indicated by the orange vertical lines and the arrows. The overlap is at charge states 26+ and 27+ with the isotopes A= $129-134$ and A= $131-136$. The data was normalized and plotted versus a digitized Hall sensor voltage equivalent to the magnetic field of the dipole magnet.

The fit function used to obtain the calibration curve is a sixth-order polynomial function. This proved to be a good set of parameters as no higher-order dependence of the residuals was visible. It is important to note that the calibration is only valid within the charge-to-mass ratio region in which xenon peaks were identified. Figure 5.8 shows

the charge-to-mass ratios plotted versus the arbitrary magnetic field and the sixth order polynomial fit to the data.

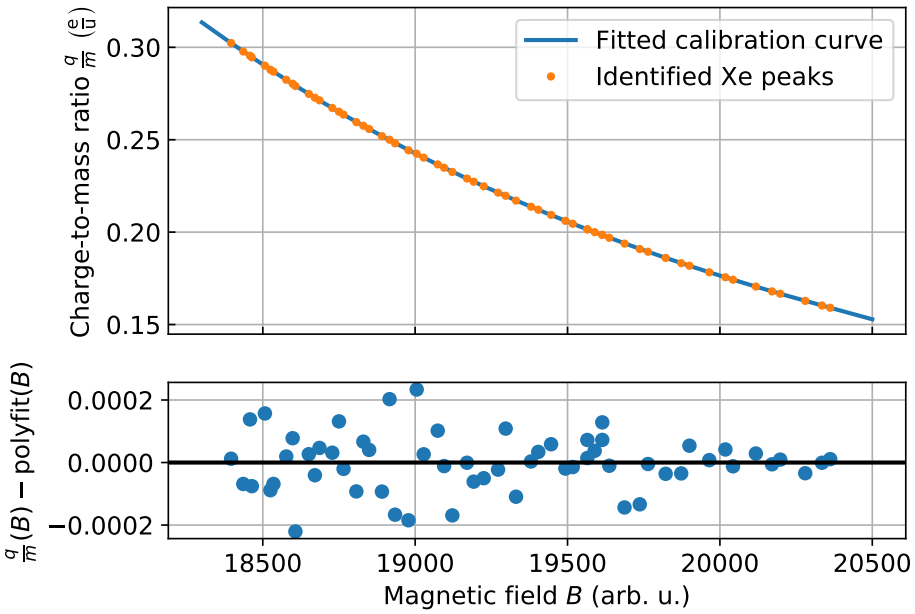

Figure 5.8: Top: Charge-to-mass ratios of the identified peaks as a function of their position along with the calibration curve. The curve can be described as a sixth-order polynomial function. **Bottom**: The residuals of the fit are visible in the lower plot. It is visible that the values are small and no higher-order dependence is present. This indicates that the order of the polynomial for the fit is sufficient.

The fit function can be used to calibrate the arbitrary magnetic field to an x-axis showing charge-to-mass ratios for spectra acquired with the same ion extraction energy. The xenon spectrum with the calibrated x-axis is displayed in Figure 5.9. Note that when calibrating the x-axis of the spectrum is inverted, since a higher magnetic field implies a lower charge-to-mass ratio.

The resulting calibration function allows to determine which elements and isotopes are ionized to which charge states, as long as the charge-to-mass ratios remain in the range in which the calibration is valid. A new calibration was necessary whenever a change was made either to the setup or to the energy with which the ions proceed through the dipole magnet. However, after adding the pulsed drift tube the energy in the beamline can be fixed, allowing to change the EBIT settings without making further calibration necessary (cf. section 4.1).

Further calibration was necessary when ions in a charge-to-mass ratio range different than xenon were to be measured or a broader magnet range was scanned. This was accomplished using the xenon spectrum as a starting point to identify the charge state of an ion at the fringe of this species' charge state distribution. For this, at least one peak of the other element had to overlap with the xenon spectrum. Following this one peak the other charge states could be identified and their peak positions plotted as a function of their charge-to-mass ratios. This data could then be fit together with the xenon positions, extending the calibrated range. Such an additional calibration was

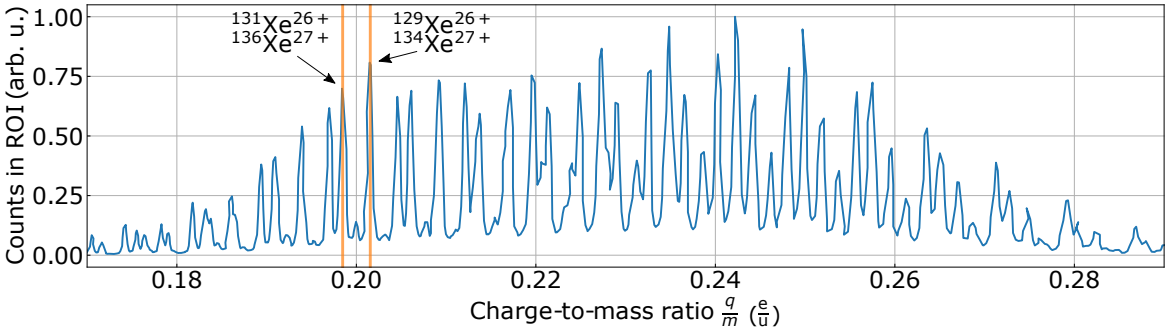

Figure 5.9: The same xenon spectrum as in Figure 5.7 is shown but with a calibrated x-axis relating the measured signal to charge-to-mass ratios. Again the isotope overlaps with which the charge states were identified are shown by orange shading and arrows.

carried out using argon, allowing a calibration of higher charge-to-mass ratios almost up to the half peak at q/m = 0.5. This peak is formed by fully ionized light rest gas ions such as $^{16}O^{8+}$ and $^{14}N^{7+}$.

5.2.2 Holmium

The first element to which the in-trap laser-induced loading technique in the Tip-EBIT was applied is holmium. It was chosen since the efficient production of HCI of ^{163}Ho for high-precision mass-ratio measurements at PENTATRAP was the initial motivation for the development of this technique. The mass ratio of ^{163}Ho and ^{163}Dy will contribute an independent Q-value of the EC decay of ^{163}Ho to the ECHo collaboration [3] which aims at the determination of the electron neutrino mass on the sub-eV level.

Throughout the work on the test setup ^{165}Ho, which is the only stable and naturally abundant isotope, was used for all holmium measurements. This isotope is readily available in an almost unlimited quantity for the development of the new in-trap laser-induced loading technique, opposed to the isotope of interest for the mass-ratio measurement, ^{163}Ho, which has to be produced e.g. in a reactor.

Macroscopic holmium target

The first holmium spectra were measured with a target containing a macroscopic amount of natural holmium. This was realized by spot-welding a holmium foil onto a titanium plate fixed to a titanium wire Figure 5.1. After successful loading, ionization, and extraction of holmium with this target, shown by an acquired charge-to-mass ratio spectrum, smaller targets were tested with sample sizes as small as 10^{10} atoms. The targets containing such limited amounts of material are produced at the institute for nuclear chemistry in Mainz with the Drop-on-Demand ink-jet printing method [51].

Figure 5.10 displays two curves which were measured with the macroscopic target inserted into the EBIT. The two curves show a comparison of a measurement repeated twice, once with and once without the laser in operation, otherwise, all settings were kept constant. The spectra cover a wide range of the dipole-bender magnet thus showing charge-to-mass ratios from 0.2 to 0.5. The charge breeding time was set to 1 s and the voltages applied to the electrodes correspond to the ones in Figure 5.4.

Following the dipole magnet, the ions were detected using the FC connected to an oscilloscope via a charge amplifier. The trace of the oscilloscope was read out and averaged for ten measurement cycles, after which the amplitude was deduced as the difference of the minimum to maximum value. The amplitude corresponds to the number of ions hitting the FC. Holmium was identified by comparing the peaks to the positions predicted by the calibration.

The two charge-to-mass ratio spectra differ strongly. As expected, holmium is only observable when the laser is in operation. Additionally, the peaks attributed to light ion species such as argon and oxygen are not detected when holmium is loaded with the laser pulses. This can be attributed to evaporative cooling in the EBIT [41]. The holmium ions are heavier and higher charged and are therefore more strongly confined, causing the light ions to evaporate from the trapping region, as described in section 2.3. This demonstrates that it is possible to load, ionize and extract holmium via in-trap laser-induced loading.

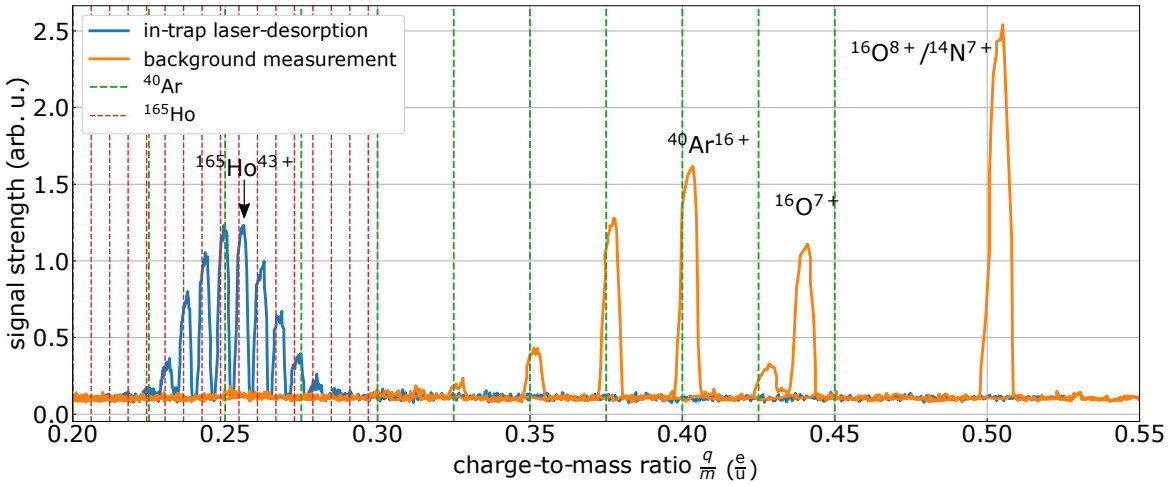

Figure 5.10: Two charge-to-mass ratio spectra measured identically except for the application of in-trap laser-induced loading. The blue curve was acquired with the laser impinging on the macroscopic holmium target, the orange curve without. The dashed red and green vertical lines show the expected positions of ^{165}Ho and ^{40}Ar charge states, respectively.

Charge state spectra of microscopic holmium targets

The smallest sample size with which a charge state spectrum of ^{165}Ho could be acquired was 10^{12} atoms. A target containing 10^{10} atoms was also tested. For this even smaller sample size, the holmium peak in the x-ray spectrum was visible, indicating that loading was accomplished. Also, for a limited amount of measurement cycles, additional signal lines were detected on the MCP. However, the signal did not surpass the background level and did not last long enough for certain identification. Thus the current lower limit of the sample size for which holmium can be loaded, ionized, and extracted is about 10^{12} atoms.

An example of charge state spectra of various sample sizes, down to the lowest of 10^{12} atoms, can be seen in Figure 5.11. For all three sample sizes (10^{16}, 10^{14}, 10^{12}

atoms), the experimental settings were identical, such as the electron beam energy (5.9 keV), the trap depth (50 V), and the charge breeding time (1 s). Nevertheless it is obvious that different charge state distributions were measured, this can be attributed to the influence of electron beam current on the charge exchange rate (cf. section 2.2), which was at about 50 mA for the two smallest targets and 37 mA for the target containing 10^{16} atoms.

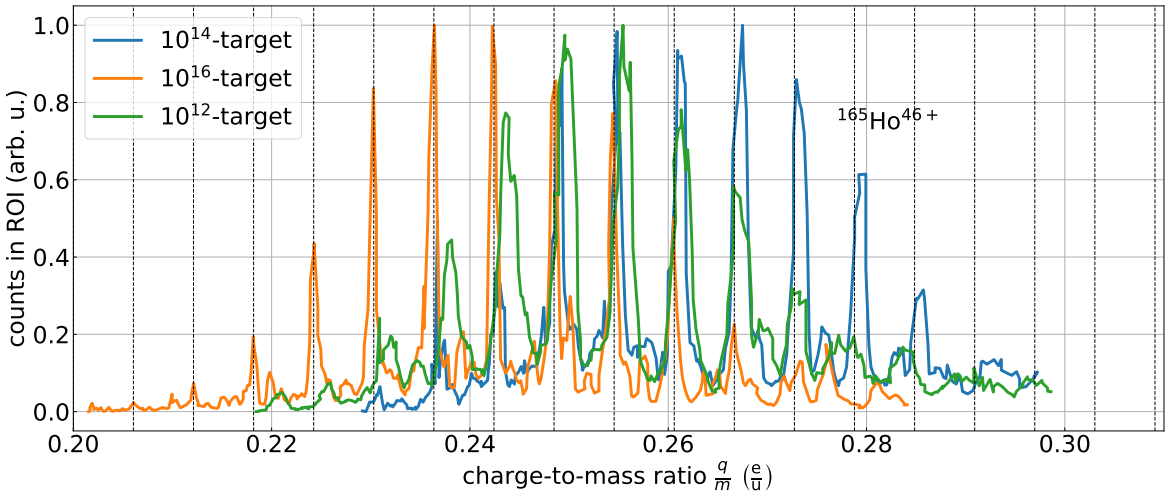

Figure 5.11: Holmium charge state spectra of targets with sample sizes of 10^{12}, 10^{14} and 10^{16} holmium atoms. The dashed vertical lines indicate the position of the holmium peaks expected due to the calibration.

Lifetime and efficiency estimate of the microscopic holmium targets

Following the successful injection of very small samples into the EBIT's trapping volume by in-trap laser desorption, the number of loading cycles for which a microscopic target can be used was estimated. In the following, this is referred to as the target lifetime. Additionally, this allows an efficiency estimate of the technique for the smallest working sample size. A sufficiently long lifetime of the targets is essential for PENTATRAP so that multiple loading cycles of the Penning traps can be performed with one target. Exchanging a target takes about 30 min but involves breaking the vacuum of the target chamber after which several hours are needed to reach a vacuum pressure at which the Tip-EBIT can be operated again.

The lifetime and the efficiency of loading, ionizing, and ejecting the ions were tested for the smallest sample size that reliably worked, which was 10^{12} holmium atoms. The current of the dipole magnet was adjusted and fixed to the value allowing the most abundant charge state, in this case Ho^{42+}, to reach the center of the detection region. The EBIT settings were the same as for the acquired charge state spectra. The holmium charge state was chosen, although Ar^{10+} has a similar charge-to-mass ratio. However, this should not influence the measurement as Figure 5.10 shows that this charge state is not ejected at these EBIT settings. Initially, lifetime measurements were carried out using only the FC. The advantage of which is that the number of ions impacting on its surface can be reliably obtained. However, temperature fluctuations in our laboratory

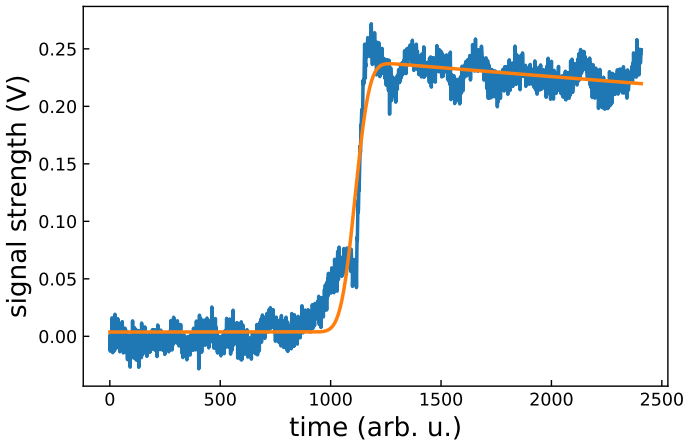

Figure 5.12: An averaged oscilloscope trace as part of the lifetime and efficiency estimate of a holmium target containing 10^{12} atoms, shown in blue. The orange curve is a fit of the fit function given in Equation (5.4).

lead to a drift of the ion spot in the detection region, possibly out of the area of the FC. The first lifetime measurements utilizing the FC showed that it is therefore not ideal for the estimation of the lifetime and efficiency. The MCP proved to be more suitable for this purpose since the detection area is larger and position sensitive. Thus a drift of the ion spot can be tracked and taken into account. However, the absolute number of ions is not deducible using only the MCP. Therefore, the first 500 measurement cycles were carried out using the FC to determine the number of ions, after which the measurement was continued with the MCP until there was almost no signal left. At this point, the FC was inserted once more to count the ions, again for about 500 measurement cycles. The ion number can thus be interpolated for the MCP measurement. To determine the background signal half of the 500 FC cycles were carried out with the laser impinging on the target and the other half without the laser, both before and after the long term MCP measurement. To account for all ions at the detector, the ion signal is focused to achieve a circular spot. The repeller electrode of the FC was set to -200 V.

For these measurements, the entire oscilloscope trace describing the discharge of the FC was acquired. While measuring, the first value of the oscilloscope trace was subtracted from all the other values of the oscilloscope trace to remove any offset. Ten such traces were averaged for a better signal to noise ratio and the averaged data was saved for analysis. The value of interest for the determination of the number of ions is the amplitude of the discharge curve. To extract this value the oscilloscope curves were fitted using the following function as an approximation for the discharge curve:

$$U(t) = A_{\mathrm{FC}} \cdot erf\left(\frac{t_0 - t}{w} + 1\right) \cdot e^{-\frac{t-t_0}{\tau}} + c\,, \tag{5.4}$$

where A_{FC} is the amplitude of the signal, $erf(\frac{t_0-t}{w} + 1)$ is an error function with the width w, the exponential describes the discharge with time constant τ, and c describes an offset of the entire function. Figure 5.12 shows an example of an oscilloscope trace fit by this function.

From the fit the signal amplitude A_{FC} in volts is extracted. Using the amplification

factor of the charge amplifier ($F_{\mathrm{amp}} = 10\,\mathrm{V/pC}$) and the charge state of the ions ($q = 42+$), the ion number impacting on the FC, N_{ions}, can be calculated as follows:

$$N_{\mathrm{ions}} = \frac{A_{\mathrm{FC}}}{F_{\mathrm{amp}}} \cdot \frac{1}{q \cdot 1.602 \cdot 10^{-19}} \,. \tag{5.5}$$

The number of ions, averaged for ten runs, with and without laser is plotted for comparison in Figure 5.13, showing the FC data before the long term MCP measurement in the upper plot and after in the lower one. The uncertainties arise from the uncertainty of the amplitude A_{FC} in the fit. The ions measured without laser are due to background gas in the EBIT. The weighted average of the ion number with and without laser are computed and then subtracted from each other to eliminate background counts. For the first FC measurement this gives an average number of ions per shot of 1039 ± 36 and for the second 55 ± 27[3], both in charge state 42+.

For the MCP measurement 10 camera frames were acquired and averaged. In this case, it is not possible to simply use a fixed ROI as with the scheme for acquiring charge state spectra, because the ion signal drifts out of this region on the time scale of the measurement. Judged by the size of the holmium ion signal an ROI with a radius of 30 pixels was chosen, which is considerably larger than for the charge state spectra. The simplest idea to track the ion spot was to find the maximum of the entire camera image, use it as the center for the region of interest and sum the signal in it. Initially, this might work out when the signal strength of the ion of interest is considerably larger than the background. As the lifetime measurement proceeds, this is not the case anymore and the ROI might follow a background signal, resulting in a false value of the holmium ion signal. Two different ways to find the maximum of the holmium signal were applied to the data. One is to give an initial position for the maximum, starting with the position in the first frame, and allow the maximum of the next image to differ in position by only a certain amount of pixels. The thus obtained new maximum position is used as the initial one for the following camera frame. This method works depending on the restraint of the distance between the initial maximum and the following one. The other method cuts a large region with a radius of 60 pixels from all the camera images. The size and position were chosen so that the holmium signal was included for every image. Then the maximum value and its position are determined in this region for each camera image, fixing the center of the ROI. In both methods, the ROI with a radius of 30 pixels is cut out with the determined maximum in the center and the counts summed up for the ion signal. The uncertainty of the total ion number of the lifetime measurement was determined by comparison of both methods which deviated by about 10%. After 50000 laser shots, the laser pulse energy was increased from 4 to 5 mJ to enhance the number of HCI and thus the signal strength.

Figure 5.14 shows the normalized counts acquired with the MCP, using the second method for finding the region of interest. The first ten data points were measured without the laser impinging on the target and their average value is set to zero when normalizing. The average value of the next ten images, which are the first ten data points for which holmium was loaded into the EBIT, is set to one. The plot shows that

[3]For both measurements the average number of ions was obtained by subtracting the values of the averages with and without laser and rounding afterwards.

the ion signal strongly decreases as the laser shots continue. After 50000 laser shots, the laser pulse energy was increased from 4 to 5 mJ to enhance the number of HCI.

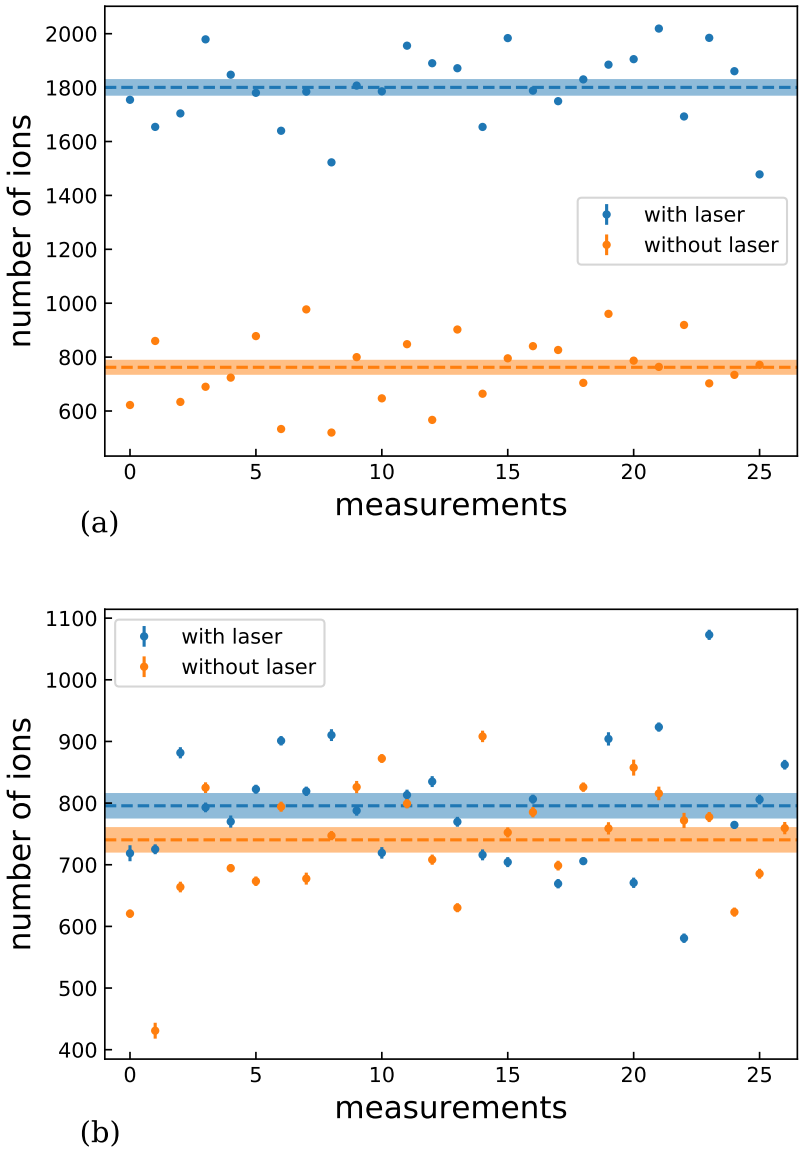

Figure 5.13: FC measurements to calibrate the MCP measurement for the lifetime and efficiency estimate of a target with a sample of 10^{12} holmium atoms. **(a)**: Quantification of the ion number before the long term MCP measurement, **(b)**: ion count afterwards. For both schemes, half of the data was taken without laser emission to determine the background signal strength. The data with laser is shown in blue, without in orange. The uncertainties arise from the uncertainty of the fit parameter A_{FC} for the discharge curve of the oscilloscope signal (cf. Equation (5.4)). For some data points the errorbars are too small to be visible. The weighted average of the ion numbers are indicated by the dashed lines for which the uncertainties are indicated by the shaded area. The weighted averages have the following values. **(a)** with laser: 1801 ± 27, without laser: 762 ± 24; **(b)** with laser: 796 ± 19, without laser: 740 ± 19.

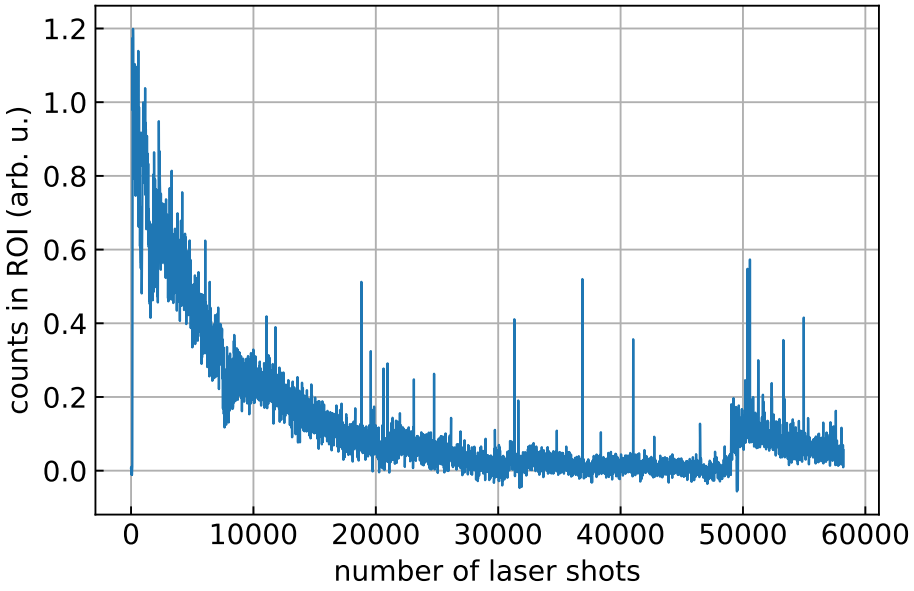

Figure 5.14: Data of the long term MCP measurement for the lifetime and efficiency estimate of a target containing 10^{12} holmium atoms. The plot shows the averaged and normalized counts per laser shot. The increase in signal after about 50000 laser shots is due to an increase in laser pulse energy from 4 to 5 mJ.

To derive the number of ions from the MCP signal a linear response of signal strength to the number of ions is assumed. For this purpose, a linear function is derived by interpolation between the first and final FC measurement, which was used to relate the ion signal of the MCP to the number of ions hitting the detector. Using this calibration function, the ion number of the long term measurement can be derived. The number of ions of the MCP measurement is plotted for the first 15000 laser shots in Figure 5.15. For the estimation of the number of ions produced in charge state 42+ only the data up to 15000 laser shots was integrated, because until this point the signal height was significantly larger than the background. For the rest of the data, the background was too high to be sure that the signal is only due to holmium ions. The total number of ions produced in the first 15000 laser shots of this measurement in charge state 42+ can be obtained as the sum of all the data up to this value. This results in a total number of ions of $(5.40 \pm 0.54) \cdot 10^6$ for the MCP measurement.

When considering that at least five thousand laser shots were fired on the target previous to the lifetime measurement on behalf of positioning of the laser and acquiring a charge state spectrum, many more HCI of holmium must have been produced. The measurement of the spectrum before the lifetime is relevant to assure the produced ion species is indeed holmium and not a contamination with a similar charge-to-mass ratio. For a conservative estimate, one can use the number of ions produced in one laser shot at the beginning of the lifetime measurement (1038 ± 36 ions per laser shot) as the ion yield per shot while acquiring the spectrum. The laser pulse energy while acquiring the spectrum was also set to 4 mJ. Since about 5000 laser shots were necessary, this results in $(5.19 \pm 0.18) \cdot 10^6$ HCI of holmium produced in charge state 42+, while acquiring the charge state spectrum for element identification. In total, this results in more than 10^7 ions of $^{165}Ho^{42+}$ and an efficiency of at least 10^{-5}, as the target contained a sample

of 10^{12} holmium atoms. This is a rough estimate of the lower limit of the number of produced ions and the efficiency presumably both are even higher.

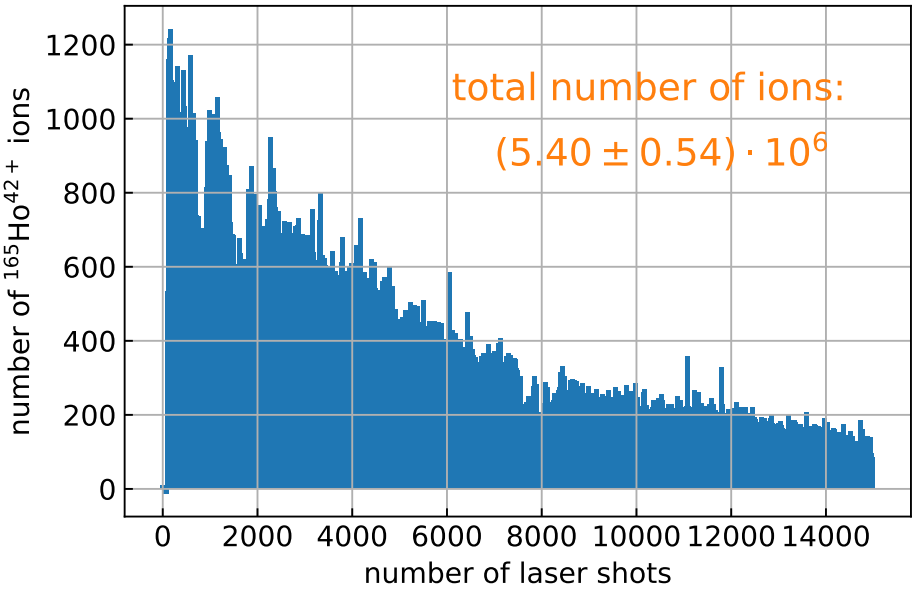

Figure 5.15: Calibrated MCP lifetime measurement of a holmium target containing 10^{12} atoms. $^{165}Ho^{42+}$ ions were detected for the measurement and the FC data before and afterwards are used for calibration. The data is displayed for the first 15000 laser shots as this is the range that is used for the estimation of the total number of $^{165}Ho^{42+}$ ions produced off the target with 10^{12} holmium atoms.

5.2.3 Other elements tested in the Tip-EBIT

In the course of this thesis also other elements were tested for the production of HCI using in-trap laser-induced loading in the Tip-EBIT. These include lead, bismuth, and calcium.

High efficiency demonstrated by lead contamination

One set of ^{165}Ho targets was contaminated with lead. As the first one was inserted into the EBIT, the mono-isotopic holmium could not be observed but instead, a heavier ion species with three abundant isotopes was detected. Using the xenon calibration performed beforehand the HCI could be identified as the three naturally abundant lead isotopes. Figure 5.16 shows a charge state spectrum of lead acquired with a contaminated holmium target. Since lead is considerably heavier than holmium, the latter cannot be trapped and ionized efficiently, because it evaporates from the trapping region. As initially the aim was to measure a holmium spectrum, the EBIT settings are the same as for the holmium measurements presented above. Considering that the lead was present only due to the contamination of a target which was supposed to contain only 10^{12} atoms, the fact that nevertheless a spectrum of lead could be acquired demonstrates the excellent efficiency of the in-trap laser-induced loading in the Tip-EBIT for heavy elements.

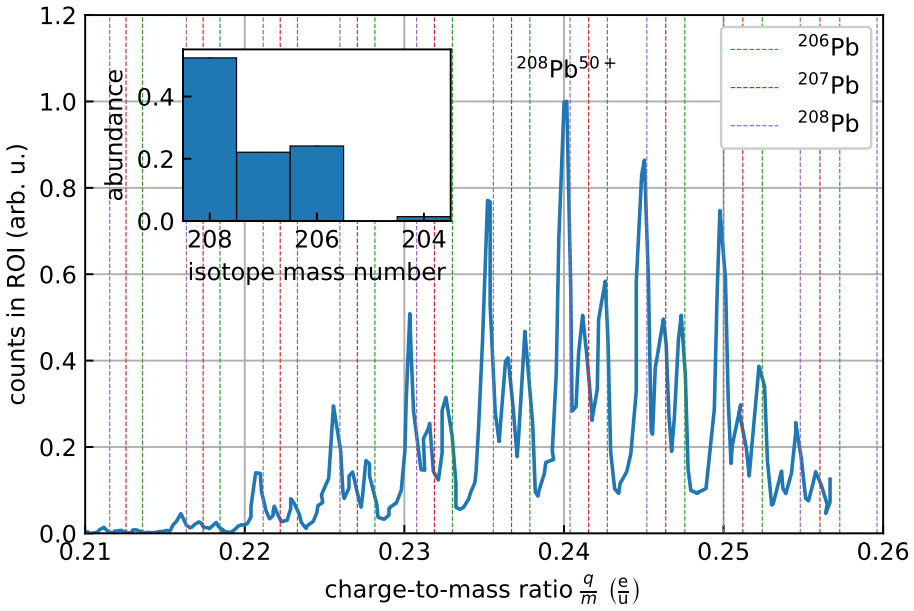

Figure 5.16: Charge state spectrum of lead acquired due to a contamination of a holmium target. The dashed vertical lines indicate the expected position of the isotope signals according to the xenon calibration. The highest peak could be associated as $^{208}Pb^{50+}$. The inset shows the isotope abundance of natural lead, data taken from [58].

Double-target test on Bi and Au

In the future at PENTATRAP, holmium and dysprosium should be loaded into adjacent Penning traps. Since the time duration for a target exchange is in the order of one day, including pumping, separate targets are not feasible. Instead, it is desirable to have both species on the same target and switch back and forth between the two elements by focusing the laser first on one sample and then on the other. To test a target containing two different species of atoms, the target with the two holes in the titanium plate was used (Figure 5.1). One hole was filled with gold the other with bismuth. These elements were chosen because they are both mono-isotopic which gives a clearer spectrum and both are rather heavy which implies easy trapping. The EBIT settings were not altered compared to the holmium measurements.

As the target was inserted into the EBIT it was accidentally dipped into the electron beam. This resulted in a strong heating of the target and sample material, due to which the bismuth melted and evaporated from the target and was dispersed in the EBIT. When aiming for HCI of bismuth this gives an excellent signal with no background, as bismuth with its high mass causes all other ions to evaporate from the trap. Bismuth has rather low melting and boiling points at atmospheric pressure (T_{melt} = 271.402°C and T_{boil} = 1564°C [60]) compared to other metals, causing the material dispersed on the surfaces inside the vacuum setup to constantly evaporate and load the EBIT with new ions. This causes a significant background signal of bismuth, even when the laser is switched off. Because of this strong contamination, no gold spectrum could be measured. Figure 5.17 shows a clear bismuth spectrum acquired when focusing the laser on the bismuth side of the target.

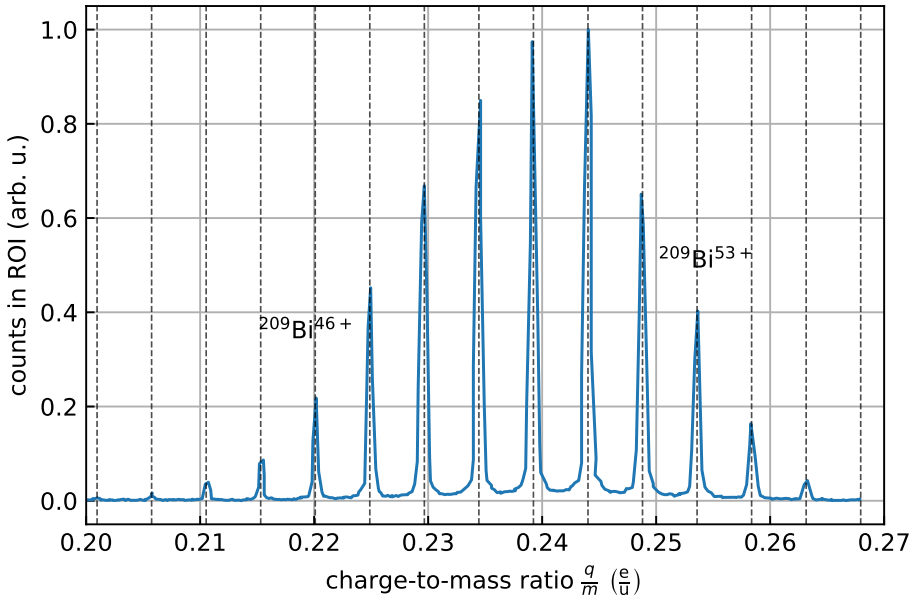

Figure 5.17: This figure shows a very clean charge state spectrum of bismuth. The most abundant charge state is $^{209}Bi^{51+}$. The dashed lines indicate where the peaks are predicted to be due to the calibration

In-trap laser desorption of light species (calcium)

Loading of calcium in the Tip-EBIT was tested mainly for two reasons. First, efficient production of HCI of calcium is of interest for future high-precision mass-measurements at PENTATRAP, requiring rare calcium isotopes for a King Plot analysis for the search of dark matter [31]. Secondly, it is rather light compared to the metals that had been tested so far and allows to test the mass range to which the new loading scheme can be applied. The same target model was used as with bismuth and gold. This time both holes were filled with calcium. Since its charge-to-mass ratio values are in a different range than for xenon, argon was used for calibration. Argon has the same atomic mass as calcium, so they cannot be differentiated in the spectra. Nevertheless, it is possible to conclude which signal is caused by HCI of calcium as the loading mechanisms differ for the two species. The differentially pumped gas injection system allows to load argon for calibration without causing residual background gas after the valve is closed. Initially, a calcium spectrum was acquired using the EBIT settings of the holmium measurements concerning the applied voltages and a charge breeding time of 100 ms, the result of which is presented in Figure 5.18. Since calcium is lighter than the previously measured elements the effect of evaporative cooling is smaller. This results in a small background signal of other ions in the measured charge state spectrum.

For future applications, such as binding energy and g-factor measurements for testing QED in strong fields [61], it was not only of interest to see if HCI of calcium can be produced but also if the production of hydrogen-like or even bare calcium is possible. To achieve such charge states a higher electron beam energy is required. It was set to 9.5 keV by setting the central drift tubes to 7 kV while the cathode remained at 2.5 kV.

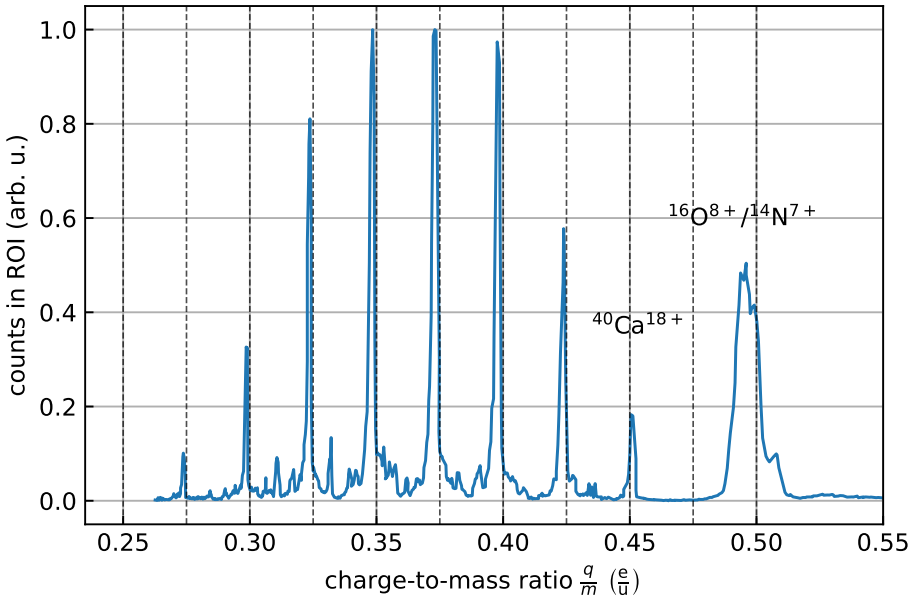

Figure 5.18: Charge state spectrum of calcium acquired using the same voltages for the electrodes of the EBIT as for holmium, an electron beam energy of 5.9 keV and a charge breeding time of 100 ms. The dashed lines show the expected positions of the calcium peaks. Since calcium is rather light compared to e.g. xenon it will not cause heavier elements to evaporate from the EBIT and thus a small background signal is visible.

The trap depth remained at 50 V. Calcium and argon spectra were acquired for charge breeding times of 100 ms and 1 s and are shown in Figure 5.19. The longer charge breeding time of 1 s was set to shift the charge state distribution to higher values. An absolute calibration at this energy was not carried out, because the mono-isotopic element argon does not have overlapping isotope peaks which would allow definite charge state identification. Nevertheless, it is possible to identify the charge states with high confidence by comparison of the calibrated low energy spectrum to the spectra at high energy of both species.

The argon spectra were acquired with the laser switched off while all other settings were the same as for the calcium measurements. For the spectrum with short charge breeding time (upper plot of Figure 5.19), the increase in electron beam energy did not result in a shift in the charge state distribution compared to the spectrum at lower electron beam energy. Considering the argon peaks related to the stripping of the s-shell electrons reveals that the first peak when one s-shell electron is removed (charge state 17+) is barely visible at the magnetic field value of 19500 arb. u, while the second one for which both s-shell electrons are removed (charge state 18+) is not reached. Accordingly, for calcium the highest charge state visible is again 18+. Comparing these spectra to the ones at a long charge breeding time of 1 s (lower plot of Figure 5.19), one can see that for both species the distribution has shifted to higher charge states. The most abundant charge states are now saturated as the gain of the MCP was in-

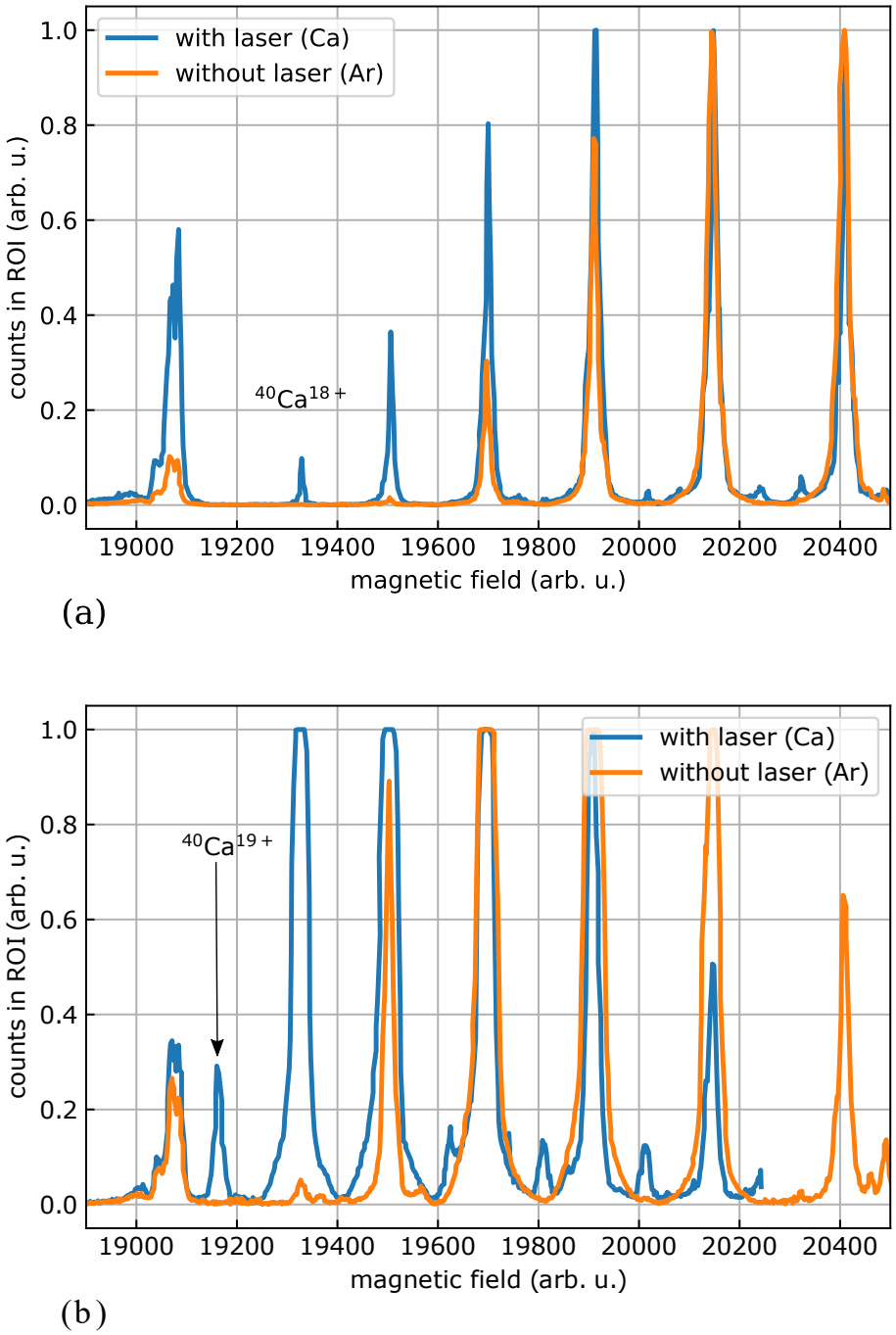

Figure 5.19: Calcium and argon charge state spectra at high electron beam energy (9.5 keV) with charge breeding times of 100 ms **(a)** and 1 s **(b)**. The measurements with the laser impinging on the target and the resulting calcium spectra are shown in blue and without laser the resulting argon spectra in orange, for both graphs. The peak at a magnetic field of 19150 arb. u. can be assigned to hydrogen-like calcium (Ca^{19+}).

creased by 60 V. The Ar^{17+} peak has increased in intensity compared to the Ar^{13+} peak, and another small peak arose which can be associated with Ar^{18+}. The same can be observed for calcium, where even Ca^{18+} is now saturated while the abundance of Ca^{14+} is reduced. Another peak arose that can be related to Ca^{19+}, which is hydrogen-like calcium. If bare calcium were produced it could not be identified since its charge-to-mass ratio would equal 0.5 and the half-peak is always abundant due to fully ionized light background gas, such as oxygen and nitrogen.

5.3 Commissioning of the newly extended Pentatrap beamline with dysprosium

The commissioning of the PENTATRAP beamline after the Tip-EBIT was attached was carried out using ^{163}Dy. This isotope was chosen because the mass ratio of HCI of ^{163}Dy and ^{163}Ho will be measured in the Penning traps. Since it is a stable isotope it is available in large quantities compared to the rare isotope ^{163}Ho. Additionally, the charge-to-mass ratios of ions of both species are the same up to the Q-value of the EC decay. This way the entire quantity of the rare holmium isotope, available to us, can be used for measurements and not for beamline optimization. Many bending, steering, and focusing voltages have to be adjusted for optimal transmission of this charge-to-mass ratio. The components are listed in subsection 4.3.2. A rough alignment of the electrostatic components can be carried out using ions from the DreEBIT. After the reconstruction of the beamline, ions produced in the DreEBIT have again successfully been trapped in the Penning traps. The dysprosium ions produced in the Tip-EBIT have reached the last MCP (MCP3) in the horizontal part of the beamline (cf. Figure 4.10).

5.4 Trouble shooting

High mass contamination

Due to evaporative cooling, contamination of low mass species does not strongly affect the production of HCI of medium-heavy elements such as holmium and dysprosium. It might shift the charge state distribution to lower values due to a higher charge exchange rate with the enhanced rest gas but can also benefit trapping by evaporatively cooling the heavier ions. Much more troublesome is a high-mass contamination, as in the case of bismuth dispersed in the EBIT. This arose due to dipping the bismuth target too far into the electron beam. In the case of bismuth, the high heat transfer to the target and sample material caused a large amount of the sample to melt and evaporate which was then dispersed in the EBIT. The first problem was increased pressure in the trapping region, resulting in lower charge states due to charge exchange which was a minor issue compared to the strong background signal of bismuth and the evaporation of all lighter species including the ions of interest.

The first approach to remove the bismuth contamination was to vent the system with nitrogen gas to about 10^{-3} mbar for a couple of hours. This was repeated three times while pumping to about 10^{-7} mbar in between, excluding the section of the elec-

tron gun which was closed off with a valve. The idea was to flush out any bismuth in the residual gas. Unfortunately, there was still a strong bismuth signal, from which was concluded that bismuth had settled on the surfaces and was out-gassing continuously. The next step was to bake out the vacuum system outside the iron yoke of the EBIT for four days at about 200°C. Again, the result was not satisfying as a pronounced bismuth signal remained, although it had decreased in strength. It was concluded that the vacuum setup had to be vented to clean possible contaminated parts of the EBIT. This involved the drift tubes and the collector. The parts were polished to mechanically remove bismuth and cleaned with isopropyl alcohol in an ultrasonic cleaner, this was repeated three times. Also, the disassembled drift tubes were baked out in a vacuum oven at about 600°C so that any residual bismuth would evaporate off the surface. Unfortunately, this resulted in a new metal coating on the ceramic parts and the metal parts were colored. The ceramic parts were again polished and cleaned in isopropyl alcohol in an ultrasonic cleaner and the metal parts were baked out again at about 900°C, both visually with a satisfying result. After assembly of all parts (cf. Figure 5.20) the vacuum setup was closed. The first spectra showed bismuth and barium. This indicated that the bismuth abundance had decreased since the lighter barium could be ionized and extracted. Barium is part of the cathode material and is emitted there. Nevertheless, the bismuth abundance was too high to use small holmium samples.

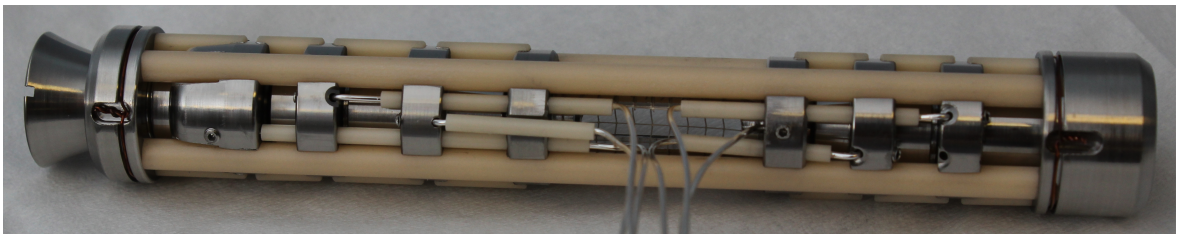

Figure 5.20: The drift tubes and ceramics after cleaning and assembly.

The section which had not been cleaned was the electron gun. To accomplish this, it was baked out while keeping the cathode heated at higher temperatures than its surroundings. Unfortunately, the result was again not satisfying.

As a final measure, a glow discharge cleaning procedure in an oxygen atmosphere was tested. In this process, the oxygen is ionized to a plasma by applying suitable voltages to the contaminated electrodes and supplying enough current, similar to a neon glow lamp. The oxygen ions are accelerated towards the negative potential and desorb contaminants from the surface [62]. The EBIT was vented with oxygen to about 1 mbar, while the electron gun was closed off with a valve. One after the other the electrodes were set to -300−-350 V. Allowing currents of 150 mA of the power supply, an oxygen plasma could be ignited at the electrode. A picture taken from a viewport is displayed in Figure 5.21. For each drift tube and the collector, the plasma was ignited for about 15 min.

Initially, it seemed that the problem was solved by the plasma cleaning since a clean xenon spectrum and a clean holmium spectrum using the macroscopic target were measured. When switching to smaller targets, the laser ablated not only holmium but again bismuth, concluding that there was a remaining bismuth contamination on the target holder which is critical if the laser is shifted next to the target and onto

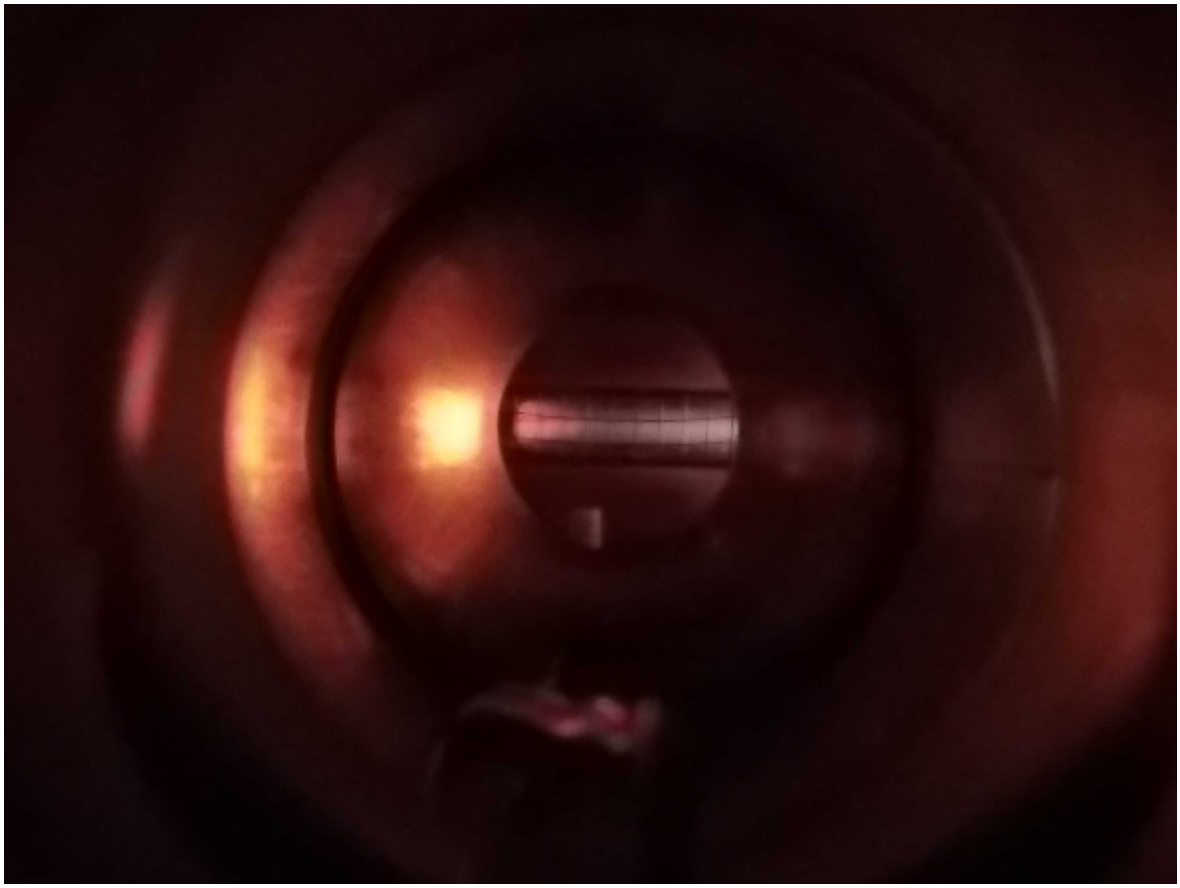

Figure 5.21: Picture taken through a viewport of the oxygen plasma used to eliminate the bismuth contamination. The plasma is visible as the white glow in the central drift tube behind the mesh wire.

the target holder. The target holder was replaced by a new one, which then finally removed the bismuth contamination.

By applying a high laser-pulse energy of several mJ to a macroscopic dysprosium target a large amount of material was distributed in the EBIT. This resulted in a contamination similar to the bismuth case. The contamination was successfully removed by applying the glow discharge cleaning process described above.

Electrical-conducting residue on the isolators

The electrodes of the electron gun as well as of the drift tubes are separated by ceramic isolators. Both areas are subject to sputtering of electrically conducting material of the electrodes (titanium, aluminum, and molybdenum) and in the case of the drift tubes also of the injected ion species and target material, such as holmium and titanium. On a long time scale, this can result in an electrically conducting layer forming on the ceramic isolators, which can be observed as increasing discharge currents on the electrodes. This can limit the applied voltage difference or even inhibit the operation of the EBIT. Since the drift tubes and ceramics were cleaned in the effort of removing the bismuth contamination this has not been an issue here, but increasing discharge currents were observed for the electron gun. In the process of moving the Tip-EBIT

to the PENTATRAP beamline, the electron gun was disassembled and the cathode was placed in a new set of electrodes and new ceramics. The newly assembled electron gun is presented in Figure 5.22. To preserve the cathode this was completed in a dry nitrogen atmosphere.

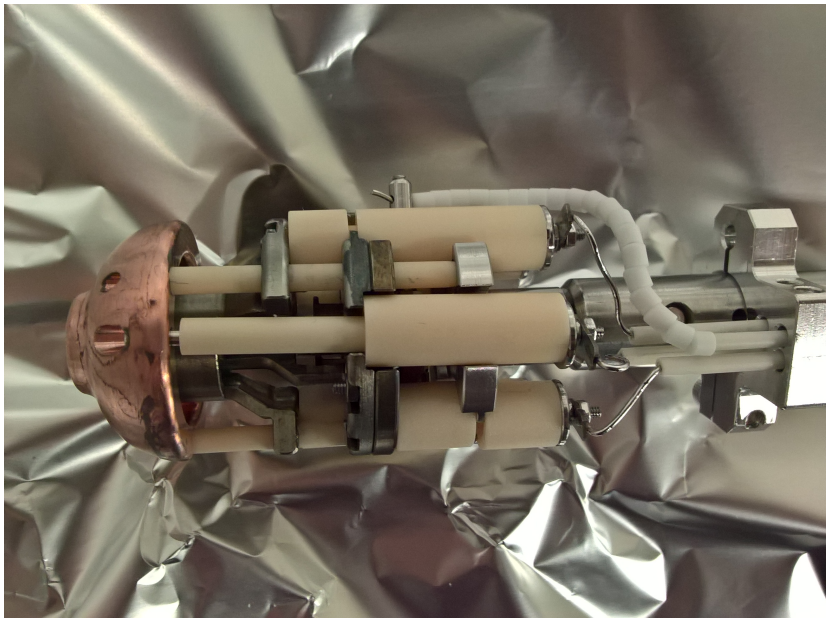

Figure 5.22: The new electron gun after assembly.

Cooling water leakage

The collector is subject to a considerable heat load due to the impacting electron beam, which is why it is water-cooled. The water feedthroughs were previously connected to the collector with bellows attached by brazing. Leakage of the cooling water supply along these bellows and especially at the brazed connection has been an issue, which increases the vacuum pressure to values at which the EBIT cannot be operated. For this reason, a new cooling design was made. The bellows are now kept as short and as straight as possible and are attached to stainless steel pipes bent at about 90° that bring the water to the collector. Additionally, in this new design the brazing could be replaced by welding. So far no leaks have occurred with this new collector design.

Chapter 6

Conclusion and Outlook

In this thesis, the optimization and commissioning of in-trap laser desorption for the loading of atoms into an HC-EBIT (Tip-EBIT) is presented. The high efficiency of this technique is demonstrated by the production and subsequent extraction of HCI using a sample containing only 10^{12} atoms of ^{165}Ho (about 270 pg), from which HCI could be produced for several ten thousand laser shots. Furthermore, the Tip-EBIT was redesigned for compatibility with the PENTATRAP beamline and for better access to the target also laser sections and a new laser setup was added. Finally, the Tip-EBIT was attached to the PENTATRAP beamline, which is currently being commissioned using the Tip-EBIT as the source for HCI. When finalized, the Tip-EBIT will serve as the source of HCI of rare isotope for high-precision mass measurements at PENTATRAP, such as ^{163}Ho for the mass-ratio measurement of ^{163}Ho and ^{163}Dy and ^{36}Cl along with ^{35}Cl for a stringent test of special relativity ($E = mc^2$).

Additionally, FAC calculations of atomic excited states and their transition strengths were carried out in a charge state range of 20+ to 31+ for holmium and 19+ to 30+ for dysprosium. This revealed atomic metastable excited states for both elements at several charge states. Based on this result the charge states for the mass measurements can be chosen to avoid a negative influence on the experimental accuracy on account of low-lying metastable states as observed in Re and Os and discussed within this thesis.

For ^{165}Ho, charge state spectra were measured using a variety of sample sizes ranging from a macroscopic holmium foil to a sample containing only 10^{12} atoms. These spectra demonstrate the production and extraction of HCI of ^{165}Ho in charge states of up to 47+. The lifetime and efficiency estimation shows that a target containing 10^{12} atoms can be used for the production of more than 10^7 HCI in a single charge state (in this case 42+). This gives an overall efficiency for loading, production, and ejection of 10^{-5} for a single charge state.

The new loading technique in the Tip-EBIT was also tested using bismuth, lead, and calcium. Bismuth demonstrates the loading technique for elements heavier than holmium, while lead was loaded due to a contamination of a target and thus emphasizes the sensitivity and the good signal-to-noise ratio of this technique for loading of small samples. The charge state spectra of calcium were acquired at varying electron beam energies and charge breeding times and show the influence of these parameters as well as the application of in-trap laser desorption for loading elements lighter than holmium. At an electron beam energy of 9.5 keV and a charge breeding time of 1 s, calcium ions

in charge states of up to 19+ (hydrogen-like calcium) could be identified.

Plasma cleaning in an oxygen environment proved to be a valuable tool for the in situ removal of unwanted contamination from the components of the EBIT in the vacuum setup. It was successfully applied to remove bismuth and later also dysprosium.

Outlook

Currently, the Tip-EBIT and the PENTATRAP beamline, to which it is now attached, are being optimized for the production, transport, and loading of HCI of ^{163}Dy into the Penning traps. This will enable the loading of HCI of this isotope and the rare ^{163}Ho into the traps for a high-precision mass-ratio measurement. The result of this measurement will lead to an independent Q_{EC}-value of the electron capture decay of ^{163}Ho to ^{163}Dy that will contribute to the goal of the ECHo-collaboration of determining the electron neutrino mass on the sub-eV level [3].

The result of the FAC calculations will help to avoid systematic shifts in the mass-ratio measurement due to low lying metastable states featured in some charge states. Additionally, such calculation can be of use for the prediction and subsequent detection of electronic transitions in Penning traps which are suitable for high-precision clocks using HCI [17].

Future measurements at PENTATRAP for which HCI of rare isotopes are required are mass measurements of calcium isotopes for dark matter search [31] and of chlorine for testing special relativity [29, 30]. However, the need for HCI of rare isotopes exceeds high-precision Penning-trap mass spectrometry and thus the possible applications of in-trap laser desorption in an EBIT in the future are numerous.

Appendix

The atomic shells considered for the excited states in the FAC calculation are listed here. For all charge states the shells 1s2 2s2 2p6 3s2 3p6 3d10 were considered as closed, $n1$ gives the ground state, followed by the possible excited state configurations. 5*1 denotes that FAC takes an excitation into any subshell of $n = 5$ into consideration.

Ho^{20+}/Dy^{19+}:
n1, 4s2 4p6 4d10 4f1
n2, 4s1 4p6 4d10 4f1 5*1
n3, 4s2 4p5 4d10 4f1 5*1
n4, 4s1 4p6 4d10 4f2
n5, 4s2 4p5 4d10 4f2
n6, 4s2 4p6 4d9 4f2
n7, 4s2 4p6 4d8 4f3
n8, 4s2 4p6 4d7 4f4

Ho^{21+}/Dy^{20+}:
n1, 4s2 4p6 4d10
n2, 4s1 4p6 4d10 5*1
n3, 4s2 4p5 4d10 5*1
n4, 4s1 4p6 4d10 4f1
n5, 4s2 4p5 4d10 4f1
n6, 4s2 4p6 4d9 4f1
n7, 4s2 4p6 4d8 4f2
n8, 4s2 4p6 4d7 4f3

Ho^{22+}/Dy^{21+}:
n1, 4s2 4p6 4d9
n2, 4s1 4p6 4d9 5*1
n3, 4s2 4p5 4d9 5*1
n4, 4s1 4p6 4d9 4f1
n5, 4s2 4p5 4d9 4f1
n6, 4s2 4p6 4d8 4f1
n7, 4s2 4p6 4d7 4f2
n8, 4s2 4p6 4d6 4f3

Ho^{23+}/Dy^{22+}:
n1, 4s2 4p6 4d8

n2, 4s1 4p6 4d8 5*1
n3, 4s2 4p5 4d8 5*1
n4, 4s1 4p6 4d8 4f1
n5, 4s2 4p5 4d8 4f1
n6, 4s2 4p6 4d7 4f1
n7, 4s2 4p6 4d6 4f2
n8, 4s2 4p6 4d5 4f3

Ho^{24+}/Dy^{23+}:
n1, 4s2 4p6 4d7
n2, 4s1 4p6 4d7 5*1
n3, 4s2 4p5 4d7 5*1
n4, 4s1 4p6 4d7 4f1
n5, 4s2 4p5 4d7 4f1
n6, 4s2 4p6 4d6 4f1
n7, 4s2 4p6 4d5 4f2
n8, 4s2 4p6 4d4 4f3

Ho^{25+}/Dy^{24+}:
n1, 4s2 4p6 4d6
n2, 4s1 4p6 4d6 5*1
n3, 4s2 4p5 4d6 5*1
n4, 4s1 4p6 4d6 4f1
n5, 4s2 4p5 4d6 4f1
n6, 4s2 4p6 4d5 4f1
n7, 4s2 4p6 4d4 4f2
n8, 4s2 4p6 4d3 4f3

Ho^{26+}/Dy^{25+}:
n1, 4s2 4p6 4d5
n2, 4s1 4p6 4d5 5*1
n3, 4s2 4p5 4d5 5*1
n4, 4s1 4p6 4d5 4f1
n5, 4s2 4p5 4d5 4f1
n6, 4s2 4p6 4d4 4f1
n7, 4s2 4p6 4d3 4f2
n8, 4s2 4p6 4d2 4f3

Ho^{27+}/Dy^{26+}:
n1, 4s2 4p6 4d4
n2, 4s1 4p6 4d4 5*1
n3, 4s2 4p5 4d4 5*1
n4, 4s1 4p6 4d4 4f1
n5, 4s2 4p5 4d4 4f1
n6, 4s2 4p6 4d3 4f1
n7, 4s2 4p6 4d2 4f2

n8, 4s2 4p6 4d1 4f3

Ho^{28+}/Dy^{27+}:
n1, 4s2 4p6 4d3
n2, 4s1 4p6 4d3 5*1
n3, 4s2 4p5 4d3 5*1
n4, 4s1 4p6 4d3 4f1
n5, 4s2 4p5 4d3 4f1
n6, 4s2 4p6 4d2 4f1
n7, 4s2 4p6 4d1 4f2
n8, 4s2 4p6 4d0 4f3

Ho^{29+}/Dy^{28+}:
n1, 4s2 4p6 4d2
n2, 4s1 4p6 4d2 5*1
n3, 4s2 4p5 4d2 5*1
n4, 4s1 4p6 4d2 4f1
n5, 4s2 4p5 4d2 4f1
n6, 4s2 4p6 4d1 4f1
n7, 4s2 4p6 4d0 4f2
n8, 4s2 4p4 4d2 4f2

Ho^{30+}/Dy^{29+}:
n1, 4s2 4p6 4d1
n2, 4s1 4p6 4d1 5*1
n3, 4s2 4p5 4d1 5*1
n4, 4s1 4p6 4d1 4f1
n5, 4s2 4p5 4d1 4f1
n6, 4s2 4p6 4d0 4f1
n7, 4s2 4p4 4d1 4f2
n8, 4s2 4p5 4d0 4f2

Ho^{31+}/Dy^{30+}:
n1, 4s2 4p6
n2, 4s1 4p6 5*1
n3, 4s2 4p5 5*1
n4, 4s1 4p6 4d1
n5, 4s2 4p5 4d1
n6, 4s1 4p6 4f1
n7, 4s2 4p5 4f1
n8, 4s2 4p4 4f2

Bibliography

[1] M. A. Levine, R. E. Marrs, J. R. Henderson, D. A. Knapp, and M. B. Schneider, "The Electron Beam Ion Trap: A New Instrument for Atomic Physics Measurements," *Physica Scripta*, vol. 1988, no. T22, p. 157, 1988. p. v, 3, 5, 9

[2] P. Micke, S. Kühn, L. Buchauer, J. R. Harries, T. M. Bücking, K. Blaum, A. Cieluch, A. Egl, D. Hollain, S. Kraemer, T. Pfeifer, P. O. Schmidt, R. X. Schüssler, C. Schweiger, T. Stöhlker, S. Sturm, R. N. Wolf, S. Bernitt, and J. R. Crespo López-Urrutia, "The Heidelberg compact electron beam ion traps," *Review of Scientific Instruments*, vol. 89, no. 6, p. 063109, 2018. p. v, 4, 19, 20

[3] L. Gastaldo, K. Blaum, K. Chrysalidis, T. Day Goodacre, A. Domula, M. Door, H. Dorrer, C. E. Düllmann, K. Eberhardt, S. Eliseev, C. Enss, A. Faessler, P. Filianin, A. Fleischmann, D. Fonnesu, L. Gamer, R. Haas, C. Hassel, D. Hengstler, J. Jochum, K. Johnston, U. Kebschull, S. Kempf, T. Kieck, U. Köster, S. Lahiri, M. Maiti, F. Mantegazzini, B. Marsh, P. Neroutsos, Y. N. Novikov, P. C. O. Ranitzsch, S. Rothe, A. Rischka, A. Saenz, O. Sander, F. Schneider, S. Scholl, R. X. Schüssler, C. Schweiger, F. Simkovic, T. Stora, Z. Szücs, A. Türler, M. Veinhard, M. Weber, M. Wegner, K. Wendt, and K. Zuber, "The electron capture in ^{163}Ho experiment – ECHo," *The European Physical Journal Special Topics*, vol. 226, pp. 1623–1694, Jun 2017. p. v, 3, 9, 40, 57

[4] T. Fang and C. R. Canizares, "Probing Cosmology with the X-Ray Forest," *The Astrophysical Journal*, vol. 539, pp. 532 – 539, 2000. p. 2

[5] P. Beiersdorfer, "Laboratory X-Ray Astrophysics," *Annual Review of Astronomy and Astrophysics*, vol. 41, no. 1, pp. 343–390, 2003. p. 2

[6] P. Beiersdorfer, "Highly charged ions in magnetic fusion plasmas: research opportunities and diagnostic necessities," *Journal of Physics B: Atomic, Molecular and Optical Physics*, vol. 48, no. 144017, 2015. p. 2

[7] S. Sturm, I. Arapoglou, A. Egl, M. Höcker, S. Kraemer, T. Sailer, B. Tu, A. Weigel, R. Wolf, J. C. López-Urrutia, and K. Blaum, "The ALPHATRAP experiment," *The European Physical Journal Special Topics*, vol. 227, pp. 1425–1491, Feb 2019. p. 2

[8] P. Beiersdorfer, "Testing QED and atomic-nuclear interactions with high-Z ions," *Journal of Physics B: Atomic, Molecular and Optical Physics*, vol. 43, p. 074032, 03 2010. p. 2

[9] M. G. Kozlov, M. S. Safronova, J. R. Crespo López-Urrutia, and P. O. Schmidt, "Highly charged ions: Optical clocks and applications in fundamental physics," *Reviews of Modern Physics*, vol. 90, 2018. p. 2

[10] J. C. Berengut, V. A. Dzuba, and V. V. Flambaum, "Enhanced Laboratory Sensitivity to Variation of the Fine-Structure Constant using Highly Charged Ions," *Physical Review Letters*, vol. 105, Sep 2010. p. 2

[11] M. Safronova, D. Budker, D. DeMille, D. F. J. Kimball, A. Derevianko, and C. W. Clark, "Search for new physics with atoms and molecules," *Reviews of Modern Physics*, vol. 90, Jun 2018. p. 2

[12] I. Bergström, C. Carlberg, T. Fritioff, G. Douysset, J. Schönfelder, and R. Schuch, "SMILETRAP—A Penning trap facility for precision mass measurements using highly charged ions," *Nuclear Instruments and Methods in Physics Research Section A: Accelerators, Spectrometers, Detectors and Associated Equipment*, vol. 487, no. 3, pp. 618 – 651, 2002. p. 2

[13] J. Dilling, P. Baartman, R. adn Bricault, M. Brodeur, L. Blomeley, F. Buchinger, J. Crawford, J. R. Crespo López-Urrutia, P. Delheij, M. Froese, G. P. Gwinner, Z. Ke, J. K. P. Lee, R. B. Moore, V. Ryjkov, G. Sikler, M. Smith, J. Ullrich, J. Vaz, and the TITAN collaboration, "Mass measurements on highly charged radioactive ions, a new approach to high precision with TITAN," *International Journal of Mass Spectrometry*, vol. 251, no. 2, pp. 198 – 203, 2006. p. 2

[14] J. Repp, C. Böhm, J. R. Crespo López-Urrutia, A. Dörr, S. Eliseev, S. George, M. Goncharov, Y. N. Novikov, C. Roux, S. Sturm, S. Ulmer, and K. Blaum, "PENTATRAP: a novel cryogenic multi-Penning-trap experiment for high-precision mass measurements on highly charged ions," *Applied Physics B*, vol. 107, no. 4, pp. 983–996, 2012. p. 2, 27, 29

[15] A. Rischka, H. Cakir, M. Door, P. Filianin, W. J. Harman, Z. ad Huang, P. Indelicato, C. H. Keitel, C. M. König, K. Kromer, M. Müller, Y. N. Novikov, R. X. Schüssler, C. Schweiger, S. Eliseev, and K. Blaum, "Mass-difference measurements on heavy nuclides with an eV/c^2 accuracy with PENTATRAP," *Physical Review Letters*, submitted, 2019. p. 2

[16] R. X. Schüssler, *First High-Precision Mass Measurements at PENTATRAP on highly charged Xe and Re ions*. Dissertation, Heidelberg University, 2019. p. 2, 12, 13

[17] R. X. Schüssler, H. Bekker, M. Brass, H. Cakir, J. C. López-Urrutia, M. Door, P. Filianin, P. Indelicato, Z. Harman, M. Haverkort, W. Huang, C. Keitel, C. M. König, K. Kromer, Y. N. Novikov, A. Rischka, C. Schweiger, S. Sturm, S. Ulmer, S. Eliseev, and K. Blaum, "Discovery of metastable states using Penning-trap mass spectrometry," in preparation, 2019. p. 2, 12, 13, 57

[18] G. Zschornack, M. Kreller, and A. Silze, "Dresden Electron Beam Ion Sources: Latest Developments," *Tech. rep.*, 2009. p. 3

[19] M. Door, "Erzeugung hochgeladener Chlor- und Siliziumionen für das Pentatrap-Experiment in einer Elektronenstrahlionenquelle unter Anwendung der MIVOC Methode.," 2015. p. 3

[20] C. Velte, F. Ahrens, A. Barth, K. Blaum, M. Brass, M. Door, H. Dorrer, C. E. Düllmann, S. Eliseev, C. Enss, P. Filianin, A. Fleischmann, L. Gastaldo, A. Goeggelmann, T. Day Goodacre, M. W. Haverkort, D. Hengstler, J. Jochum, K. Johnston, M. Keller, S. Kempf, T. Kieck, C. M. König, U. Köster, K. Kromer, F. Mantegazzini, B. Marsh, Y. N. Novikov, F. Piquemal, C. Riccio, D. Richter, A. Rischka, S. Rothe, R. Schüssler, C. Schweiger, T. Stora, M. Wegner, K. Wendt, M. Zampaolo, and K. Zuber, "High-resolution and low-background ^{163}Ho spectrum: interpretation of the resonance tails," *European Physical Journal*, submitted, 2019. p. 3

[21] M. Aker, K. Altenmüller, M. Arenz, M. Babutzka, J. Barrett, S. Bauer, M. Beck, A. Beglarian, J. Behrens, T. Bergmann, U. Besserer, K. Blaum, F. Block, S. Bobien, K. Bokeloh, J. Bonn, B. Bornschein, L. Bornschein, H. Bouquet, T. Brunst, T. S. Caldwell, L. L. Cascio, S. Chilingaryan, W. Choi, T. J. Corona, K. Debowski, M. Deffert, M. Descher, P. J. Doe, O. Dragoun, G. Drexlin, J. A. Dunmore, S. Dyba, F. Edzards, L. Eisenblätter, K. Eitel, E. Ellinger, R. Engel, S. Enomoto, M. Erhard, D. Eversheim, M. Fedkevych, A. Felden, S. Fischer, B. Flatt, J. A. Formaggio, F. M. Fränkle, G. B. Franklin, H. Frankrone, F. Friedel, D. Fuchs, A. Fulst, D. Furse, K. Gauda, H. Gemmeke, W. Gil, F. Glück, S. Görhardt, S. Groh, S. Grohmann, R. Grössle, R. Gumbsheimer, M. H. Minh, M. Hackenjos, V. Hannen, F. Harms, J. Hartmann, N. Haußmann, F. Heizmann, K. Helbing, S. Hickford, D. Hilk, B. Hillen, D. Hillesheimer, D. Hinz, T. Höhn, B. Holzapfel, S. Holzmann, T. Houdy, M. A. Howe, A. Huber, A. Jansen, A. Kaboth, C. Karl, O. Kazachenko, J. Kellerer, N. Kernert, L. Kippenbrock, M. Kleesiek, M. Klein, C. Köhler, L. Köllenberger, A. Kopmann, M. Korzeczek, A. Kosmider, A. Kovalí, B. Krasch, M. Kraus, H. Krause, L. Kuckert, B. Kuffner, N. Kunka, T. Lasserre, T. L. Le, O. Lebeda, M. Leber, B. Lehnert, J. Letnev, F. Leven, S. Lichter, V. M. Lobashev, A. Lokhov, M. Machatschek, E. Malcherek, K. Müller, M. Mark, A. Marsteller, E. L. Martin, C. Melzer, A. Menshikov, S. Mertens, L. I. Minter, S. Mirz, B. Monreal, P. I. M. Guzman, K. Müller, U. Naumann, W. Ndeke, H. Neumann, S. Niemes, M. Noe, N. S. Oblath, H. W. Ortjohann, A. Osipowicz, B. Ostrick, E. Otten, D. S. Parno, D. G. P. II, P. Plischke, A. Pollithy, A. W. P. Poon, J. Pouryamout, M. Prall, F. Priester, M. Röllig, C. Röttele, P. C. O. Ranitzsch, O. Rest, R. Rinderspacher, R. G. H. Robertson, C. Rodenbeck, P. Rohr, C. Roll, S. Rupp, M. Rysavy, R. Sack, A. Saenz, P. Schäfer, L. Schimpf, K. Schlösser, M. Schlösser, L. Schlüter, H. Schön, K. Schönung, M. Schrank, B. Schulz, J. Schwarz, H. Seitz-Moskaliuk, W. Seller, V. Sibille, D. Siegmann, A. Skasyrskaya, M. Slezak, A. Spalek, F. Spanier, M. Steidl, N. Steinbrink, M. Sturm, M. Suesser, M. Sun, D. Tcherniakhovski, H. H. Telle, T. Thümmler, L. A. Thorne, N. Titov, I. Tkachev, N. Trost, K. Urban, D. Venos, K. Valerius, B. A. VanDevender, R. Vianden, A. P. V. Hernandez, B. L. Wall, S. Wüstling, M. Weber, C. Weinheimer, C. Weiss, S. Welte, J. Wendel, K. J. Wierman, J. F. Wilkerson, J. Wolf, W. Xu, Y. R. Yen, M. Zacher, S. Zadorozhny, M. Zboril, and

G. Zeller, "An improved upper limit on the neutrino mass from a direct kinematic method by KATRIN," no. 1909.06048, 2019. p. 3

[22] Y. A. Litvinov and F. Bosch, "Beta decay of highly charged ions," *Reports on Progress in Physics*, vol. 74, p. 016301, dec 2010. p. 3

[23] J. D. Gillaspy, "Highly charged ions," *Journal of Physics B: Atomic, Molecular and Optical Physics*, vol. 34, pp. R93–R130, sep 2001. p. 3

[24] U. Feldman, M. Swartz, and L. Cohen, "Vacuum Ultraviolet Source," *Review of Scientific Instruments*, vol. 38, no. 1372, 1967. p. 3

[25] R. Geller, "New High Intensity Ion Source with Very Low Extraction Voltage," *Applied Physics Letters*, vol. 16, no. 401, 1970. p. 3

[26] E. D. Donets, "Electron Beam Ion Sources and Associated Physics at JINR," *Nuclear Instruments and Methods in Physics Research*, pp. 522–525, 1985. p. 3

[27] S. R. Elliot and R. E. Marrs, "A wire probe as an ion source for an electron beam ion trap," *Nuclear Instruments and Methods in Physics Research Section B: Beam Interactions with Materials and Atoms*, vol. 100, no. 4, pp. 529 – 535, 1995. p. 4

[28] Ch. Schweiger, "Construction and commissioning of a room-temperature electron beam ion trap and development of a wire probe injection system," master thesis, Heidelberg University, 2017. p. 4, 6, 8, 21, 22

[29] S. Rainville, J. K. Thompson, E. G. Myers, J. M. Brown, M. S. Dewey, E. G. Kessler Jr., R. D. Deslattes, H. G. Brörner, M. Jentsche, P. Mutti, and D. E. Pritchard, "A direct test of E=mc^2," *Nature*, vol. 438, Dec 2005. p. 4, 57

[30] M. Jentschel and K. Blaum, "Balancing energy and mass with neutrons," *Nature*, vol. 14, May 2018. p. 4, 57

[31] J. C. Berengut, D. Budker, C. Delaunay, V. V. Flambaum, C. Frugiuele, E. Fuchs, C. Grojean, R. Harnik, R. Ozeri, G. Perez, and Y. Soreq, "Probing New Long-Range Interactions by Isotope Shift Spectroscopy," *Phys. Rev. Lett.*, vol. 120, p. 091801, Feb 2018. p. 4, 49, 57

[32] M. A. Levine, R. E. Marrs, J. N. Bardsley, P. Beiersdorfer, C. L. Bennett, M. H. Chen, T. Cowan, D. Dietrich, J. R. Henderson, D. A. Knapp, A. Osterheld, B. M. Penetrante, M. B. Schneider, and J. H. Scofield, "The use of an electron beam ion trap in the study of highly charged ions," *Nuclear Instruments and Methods in Physics Research Section B: Beam Interactions with Materials and Atoms*, vol. 43, no. 3, pp. 431–440, 1989. p. 5, 9

[33] R. E. Marrs, S. R. Elliott, and D. A. Knapp, "Production and Trapping of Hydrogenlike and Bare Uranium Ions in an Electron Beam Ion Trap," *Physical Review Letters*, vol. 72, pp. 4082–4085, Jun 1994. p. 5, 9

[34] R. F. Steinbrügge, *Bestimmung von absoluten Auger- und radiativen Zerfallsraten K-Schalen-angeregter hochgeladener Eisenionen*. Dissertation, Heidelberg University, 2015. p. 6

[35] W. Lotz, "An empirical formula for the electron-impact ionization cross-section," *Zeitschrift für Physik*, vol. 206, no. 2, pp. 205–211, 1967. p. 7, 8

[36] G. Herrmann, "Optical Theory of Thermal Velocity Effects in Cylindrical Electron Beams," *Journal of Applied Physics*, vol. 29, no. 2, pp. 127–136, 1958. p. 7

[37] F. Currell and G. Fussmann, "Physics of electron beam ion traps and sources," *IEEE Transactions on Plasma Science*, vol. 33, pp. 1763–1777, Dec 2005. p. 7

[38] L. Brillouin, "A Theorem of Larmor and Its Importance for Electrons in Magnetic Fields," *Physical Review*, vol. 67, pp. 260–266, Apr 1945. p. 7

[39] A. Kramida, Yu. Ralchenko, J. Reader, and and NIST ASD Team. NIST Atomic Spectra Database (ver. 5.7), [Online]. Available: `http://physics.nist.gov/asd` [2019, October 15]. National Institute of Standards and Technology, Gaithersburg, MD., 2019. p. 8, 14

[40] J. D. Gillaspy, *Trapping Highly Charged Ions: Fundamentals and Applications*. Nova Science Publishers, Inc., 2001. p. 7, 9

[41] M. B. Schneider, M. A. Levine*, C. L. Bennett, J. R. Henderson, D. A. Knapp, and R. E. Marrs, "Evaporative cooling of highly charged ions in EBIT: An experimental realization," *AIP Conference Proceedings*, vol. 188, no. 1, pp. 158–165, 1989. p. 9, 41

[42] E. U. Condon and S. G. H, *The theory of atomic spectra*. Cambridge University Press, 1935. p. 13

[43] J. C. Berengut, V. A. Dzuba, V. V. Flambaum, and A. Ong, "Highly charged ions with E1, M1, and E2 transitions within laser range," *Physical Review A*, vol. 86, Aug 2012. p. 14

[44] M. F. Gu, "The flexible atomic code," *Canadian Journal of Physics*, vol. 86, pp. 675–689, sep 2008. p. 15

[45] M. F. Gu, "FAC 1.1.5 Manual," p. 15, 16, 18

[46] P. Indelicato, F. Parente, and R. Marrus, "Effect of hyperfine structure on the 2 $^3P_1$ and the 2 $^3P_0$ lifetime in heliumlike ions," *Phys. Rev. A*, vol. 40, pp. 3505–3514, Oct 1989. p. 16

[47] P. Indelicato, "Private communication," 2019. p. 17

[48] Spectra-Mat, Inc., *Guidelines for Processing of Dispenser Cathodes*. Spectra-Mat, Inc., 2018. p. 20

[49] Behlke Power Electronics GmbH, *High voltage puch-pull switching units*. Behlke Power Electronics GmbH, 2019. p. 21, 22

[50] Ch. Schweiger, J. R. C. López-Urrutia, M. Door, H. Dorrer, Ch. E. Düllmann, S. Eliseev, P. Filianin, W. Huang, C. M. König, K. Kromer, M. Müller, D. Renisch, A. Rischka, R. X. Schüssler, and K. Blaum, "Production of highly-charged ions of rare species by in-trap laser-induced desorption inside an electron beam ion trap," *Review of Scientific Instruments*, submitted 2019. p. 25

[51] R. Haas, S. Lohse, C. Düllmann, K. Eberhardt, C. Mokry, and J. Runke, "Development and characterization of a Drop-on-Demand inkjet printing system for nuclear target fabrication," *Nuclear Instruments and Methods in Physics Research Section A: Accelerators, Spectrometers, Detectors and Associated Equipment*, vol. 874, pp. 43–49, 2017. p. 26, 32, 40

[52] L. Gastaldo, K. Blaum, A. Doerr, C. E. Düllmann, K. Eberhardt, S. Eliseev, C. Enss, A. Faessler, A. Fleischmann, S. Kempf, M. Krivoruchenko, S. Lahiri, M. Maiti, Y. N. Novikov, P. C.-O. Ranitzsch, F. Simkovic, Z. Szusc, and M. Wegner, "The Electron Capture ^{163}Ho Experiment ECHo," *Journal of Low Temperature Physics*, vol. 176, pp. 876–884, Sep 2014. p. 28

[53] K. Blaum, "High-accuracy mass spectrometry with stored ions," *Physics Reports*, vol. 425, no. 1, pp. 1 – 78, 2006. p. 28

[54] C.-E. Roux, *High-Resolution Mass Spectrometry: The Trap Design and Detection System of Pentatrap and New Q-Values for Neutrino Studies*. Dissertation, Heidelberg University, 2012. p. 28

[55] L. S. Brown and G. Gabrielse, "Precision spectroscopy of a charged particle in an imperfect Penning trap," *Physical Review A*, vol. 25, pp. 2423–2425, Apr 1982. p. 29

[56] D. J. Wineland and H. G. Dehmelt, "Principles of the stored ion calorimeter," *Journal of Applied Physics*, vol. 46, no. 2, pp. 919–930, 1975. p. 29

[57] P. B. Johnson and R. W. Christy, "Optical constants of transition metals: Ti, V, Cr, Mn, Fe, Co, Ni, and Pd," *Phys. Rev. B*, vol. 9, pp. 5056–5070, Jun 1974. p. 33, 34

[58] J. R. de Laeter, J. K. Böhlke, P. D. Biévre, H. Hidaka, H. S. Peiser, K. J. R. Rosman, and P. D. P. Taylor, "Atomic weights of the elements," *IUPAC: Pure and Applied Chemistry*, vol. 75, no. 6, pp. 683–800, 2000. p. 34, 38, 48

[59] R. Jordan, D. Cole, J. G. Lunney, K. Mackay, and D. Givord, "Pulsed laser ablation of copper," *Applied Surface Science*, vol. 86, pp. 24–28, 1995. p. 34

[60] J. R. Rumble, ed., *"Summary of Properties of the Elements", CRC Handbook of Chemistry and Physics*. CRC Press/Taylor and Francis, Boca Raton, FL., 2019. p. 48

[61] F. Köhler, K. Blaum, M. Block, S. Chenmarev, S. Eliseev, D. A. Glazov, M. Goncharov, J. Hou, A. Kracke, D. A. Nesterenko, Y. N. Novikov, Q. Wolfgang, E. Minaya Ramirez, V. M. Shabaev, S. Sturm, A. V. Volotka, and G. Werner, "Isotope

dependence of the Zeeman effect in lithium-like calcium," *Nature Communications*, vol. 7, no. 10246, 2016. p. 49

[62] J. Engler, D. Moucka, and J. Wochele, "Glow discharge cleaning of stainless steel surfaces for ionization chambers," *Nuclear Instruments and Methods in Physics Research Section B: Beam Interactions with Materials and Atoms*, vol. 100, no. 1, pp. 183–187, 1994. p. 53

Declaration

Ich versichere, dass ich diese Arbeit selbstständig verfasst und keine anderen als die angegebenen Quellen und Hilfsmittel benutzt habe.

Heidelberg, den ,

Charlotte König